Submitted to *Physics of Fluids*

The role of scalar forcing in direct numerical simulations of turbulent atmospheric clouds

Abdullah Al Muti Sharfuddin,[1] Foluso Ladeinde,[1,a)] Yangang Liu,[2] Fan Yang,[2] Mohammad Atif,[3] Tao Zhang,[2] Wenhai Li,[4] Meifeng Lin,[3] and HyeJin Oh[1]

[1]*Department of Mechanical Engineering, 113 Light Engineering Building, Stony Brook University, 100 Nicolls Road, Stony Brook, New York, 11794-2300, USA*

[2]*Environmental and Climate Sciences Department, Brookhaven National Laboratory, 2 Center St, Upton, New York, 11973-5000, USA*

[3]*Computational Science Initiative, Brookhaven National Laboratory, 2 Center St, Upton, New York, 11973-5000, USA*

[4]*Department of Mechanical Engineering Technology, Farmingdale State College, 2350 Broadhollow Road, Farmingdale, New York, 11735-1021, USA*

Direct numerical simulation (DNS) is a promising approach to fill knowledge gaps regarding the microscale evolution of turbulent clouds. The governing equations for the flow of ambient air are solved in Eulerian framework, assuming homogeneous and isotropic turbulence. Two scalar fields, namely temperature and vapor mixing ratio, are transported by the turbulent velocity field. The aerosol particles and cloud droplets are tracked in Lagrangian fashion. It is known that forcing is required to sustain turbulence in a DNS model. Although momentum forcing is common in DNS studies of clouds, forcing of the scalar fields has not gained enough attention. The present work implements forcing in both momentum and scalar fields and simulates mixing between the cloud and environment. Our results show that forcing drives the mean scalar fields to equilibrium faster and suppresses microscale phase change. While fluctuations in the scalar fields are sustained by forcing, probability distributions of the forced scalar fields become non-Gaussian. It is found that scalar forcing counteracts homogenization of the scalar fields caused by flow turbulence. Both momentum and scalar forcings affect scalar fluctuations and thereby influence the microphysics of cloud droplets and aerosol particles. The scalar fields, being coupled with particles, have reduced diffusivity and their spectra include a viscous-convective regime which is further widened if forcing is applied. It is shown that scalar forcing is needed in a DNS model to maintain thermodynamic fluctuations as observed in natural clouds.

[a)] Author to whom correspondence should be addressed. Electronic mail: Foluso.Ladeinde@Stonybrook.edu

NOMENCLATURE

α	= imposed scalar variance [K^2 for temperature and $(g/kg)^2$ for vapor mixing ratio]
β	= mean scalar gradient [K/m for temperature and g/kgm for vapor mixing ratio]
c_p, C_d	= specific heat of air [J/(kg.K)], rate of condensation or evaporation [1/s]
δ_{k,k_f}, δ_T, δ_{q_v}	= delta functions [-] in the Fourier space, temperature field, and vapor field, respectively
$\epsilon_{T,in}$, $\epsilon_{q_v,in}$	= dissipation rates in the initial temperature [K^2/s], and vapor [$(g/kg)^2/s$] fields
ϵ, η	= turbulent kinetic energy dissipation rate [m^2/s^3], Kolmogorov scale [m]
η_B, E_T, E_{q_v}	= Bachelor scale [m], temperature spectrum [K^2m], vapor spectrum [$(g/kg)^2m$]
$\boldsymbol{F}_b$, $\boldsymbol{F}_c$	= buoyancy force [N], external force in the momentum field [N]
F_T, F_{q_v}	= external force in the temperature field [N], external force in the vapor field [N]
$\boldsymbol{g}$, $\boldsymbol{k}_f$	= acceleration vector due to gravity [m/s^2], forcing wavenumber vector [1/m]
k_{min}, k_{max}	= minimum wavenumber [1/m], maximum wavenumber [1/m]
κ, k_T	= hygroscopicity of solute [-], thermal conductivity in air [W/(m.K)]
L_h, λ, M_l	= specific latent heat [J/kg], Taylor microscale [m], molar mass of water [kg/mol]
m_a, μ_T, μ_v	= mass of air [kg], molecular diffusivities [m^2/s] of temperature, water vapor in air
ν, p	= kinematic viscosity of air [m^2/s], instantaneous fluid pressure [N/m^2]
q_v, $q_{v,s}$	= instantaneous water vapor mixing ratio [g/kg], saturation vapor mixing ratio [g/kg]
r_d, r	= dry aerosol radius [μm], wet radius of aerosol particle or cloud droplet [μm]
r_c, R_v	= critical radius [μm], specific gas constant for water vapor [J/(kg.K)]
$R_{q_v'q_v'}$	= auto-correlation coefficient for fluctuating water vapor mixing ratio [-]
ρ_a, ρ_l, S_e	= density of air [kg/m^3], density of water [kg/m^3], environmental supersaturation [-]
S_k, S_c	= particle equilibrium supersaturation [-], critical equilibrium supersaturation [-]
Sc, σ_l	= Schmidt number [-], surface tension of water [N/m]
T, τ_p	= instantaneous temperature [K], particle response time [s]
$\boldsymbol{u}$, u_{rms}	= instantaneous fluid velocity vector [m/s], root-mean-square velocity [m/s]
$\boldsymbol{V}$, $\boldsymbol{X}$	= particle velocity vector [m/s], particle position vector [m]
PDF, TKE	= probability density function [-], turbulent kinetic energy [m^2/s^3]

I. INTRODUCTION

Numerical modeling has become indispensable to study turbulence-cloud-aerosol interactions in the atmosphere since experimental measurements are few and difficult to conduct. The most accurate computational approach is direct numerical simulation (DNS) coupled with Lagrangian particle tracking. This method resolves the flow of turbulent air upto the smallest scale without any kind of turbulence modeling and tracks cloud droplets and aerosol particles individually in Lagrangian fashion.[1] Two thermodynamic (scalar) fields, namely temperature and vapor mixing ratio, are transported in Eulerian framework. DNS models rely on a forcing mechanism to maintain turbulent fluctuations.[2] Many DNS studies (Vaillancourt et al.,[1] Kumar et al.,[3] and Yu Li et al.[4]) and our previous DNS model (Gao et al.[5] and Sharfuddin et al.[6]) applied forcing in the momentum field only. While turbulence was sustained in the velocity field, fluctuations in the scalar fields decayed in those models. However, convective motion, radiative effects, and phase change (latent heat release) sustain thermodynamic fluctuations in real clouds.[7] In the present study, we add forcing in the scalar fields to sustain fluctuations at desired levels. The aim is to realistically simulate a region within the cloud where thermodynamic fluctuations are strong.

Without a turbulence production mechanism, turbulence decays in a numerical model and therefore an external forcing is needed. Eswaran and Pope[2] demonstrated that forcing in the Fourier space produces a statistically stationary velocity field. Janin et al.[8] implemented linear forcing in the physical space to maintain homogeneous and isotropic turbulence (HIT). Fourier forcing is applied to a band of low wavenumbers in the Fourier space, but linear forcing is carried out in the physical space with energy injected at all nodal points. Besides momentum forcing, many previous studies have applied forcing in the scalar fields to prevent the decay of scalar fluctuations. Overholt and Pope[9] applied mean gradient forcing in the physical space and showed that the fluctuating scalar field reaches a statistically stationary state. Gotoh and Watanabe[10] implemented mean gradient forcing in a passive scalar field transported by HIT. Daniel et al.[11] proposed a forcing term in the physical space based on chemical reaction analogy and showed that this approach keeps the scalar field within a predefined bound. Chen and Cao,[12] Watanabe and Gotoh,[13] and Kerr[14] carried out scalar forcing in a band of low wavenumbers in the Fourier space. Carroll et al.[15] adopted physical-space linear forcing that imposes a scalar variance and tested it for a range of Schmidt numbers. In the context of atmospheric clouds, Paoli and Shariff[16] applied Fourier forcing in the temperature and vapor mixing ratio fields in addition to the momentum field. Chen et al.[17] forced the scalar fields in a low wavenumber band to study the evolution of mixed-phase clouds.

Scalar forcing plays an important role at the small scales if scalar fields are coupled with particles. Satio et al.[18] examined the relationship between scalar fluctuations and particles using a DNS model with Fourier scalar forcing. The authors reported that the TKE spectrum decays rapidly in the dissipation scale as expected in HIT, but the scalar spectrum remains flat in the intermediate and dissipation scales. They attributed modification of the scalar spectrum to the presence of particles that are smaller than the Kolmogorov length. Pumir[19] investigated the scale dependence of scalar fluctuations using DNS and mean scalar gradient forcing for a range of Prandtl numbers but excluded particles. The scalar spectra differ at all scales, including the small scales, and are different in the directions perpendicular and parallel to the mean gradient. However, the spectral profiles follow a slope of -5/3 and no flattening is observed in the inertial subrange due to the absence of particles. The Schmidt number is less than unity for atmospheric flows, but the finite mass of cloud droplets and aerosol particles increases the effective Schmidt number.[20] By applying a DNS model and Fourier forcing in the scalar fields, Watanabe and Gotoh[13] studied the transport of a passive scalar field for which the Schmidt number is unity. The authors reported the existence of a viscous-convective subrange between the inertial and dissipation ranges.

Critical knowledge gap exists regarding the role of scalar forcing in DNS models that simulate microscale cloud processes such as condensation, activation, evaporation, and deactivation.[6] Hence, we extend our previous DNS model[6] to include forcing in the temperature and vapor mixing ratio fields. Three scalar forcing techniques: Fourier, mean gradient and linear, are implemented. Previous models[9,10,13,15] that included scalar forcing lacked the coupling between scalar fields and particles. We examine the interaction between forced scalar fields and particles at large, intermediate, and small scales. Unlike the models of Paoli and Shariff[16] and Chen et al.[17], our initial setup consists of two regions with distinct supersaturation levels. This allows us to simulate mixing between the cloud and clear air. We also vary the intensity of flow turbulence and discuss the impact on scalar fields and microphysics.

II. GOVERNING EQUATIONS

The equations solved in our model are described in this section. They include the Navier-Stokes equations, the scalar transport equations with forcing methods in the physical and Fourier spaces, and the equations for Lagrangian particle tracking.

A. Turbulent velocity field

The turbulent air in the atmosphere is assumed to be governed by the physical-space Navier-Stokes equations with the Boussinesq approximation:[21]

$$\frac{\partial \boldsymbol{u}}{\partial t} + (\boldsymbol{u}.\nabla)\boldsymbol{u} = -\frac{1}{\rho_a}\nabla p + \nu\nabla^2\boldsymbol{u} + \boldsymbol{F}_b + \boldsymbol{F}_c\,, \tag{1}$$

$$\nabla.\boldsymbol{u} = 0\,. \tag{2}$$

Here, $\boldsymbol{u}$ is the instantaneous fluid velocity vector and p is the instantaneous fluid pressure, $\boldsymbol{F}_b$ is the buoyancy force, and $\boldsymbol{F}_c$ is the external force applied to sustain flow turbulence. The definitions of $\boldsymbol{F}_b$ and $\boldsymbol{F}_c$ can be found in Ref. 6.

B. Scalar transport and scalar forcing

The thermodynamic variables or scalar quantities in this problem are temperature, water vapor mixing ratio, and supersaturation. The transport equations for temperature and water vapor mixing ratio fields are written in the Eulerian framework as:[5]

$$\frac{\partial T}{\partial t} + (\boldsymbol{u}.\nabla)T = \frac{L_h}{c_p}C_d + \mu_T\nabla^2 T + \delta_T F_T\,, \tag{3}$$

$$\frac{\partial q_v}{\partial t} + (\boldsymbol{u}.\nabla)q_v = -C_d + \mu_v\nabla^2 q_v + \delta_{q_v}F_{q_v}\,. \tag{4}$$

where C_d quantifies the time rate of mass exchange between liquid water and water vapor and is described by Eq. (24). The C_d is positive during condensation and negative during evaporation. The terms $L_h C_d/c_p$ and $-C_d$ are latent heat terms in Eqs. (3) and (4), respectively. The F_T and F_{q_v} are the forcing terms for temperature and water vapor mixing ratio, respectively; and the δ_T and δ_{q_v} are the delta functions defined as

$$\delta_T = \begin{cases} 1 & if\ \dfrac{L_h}{c_p}C_d > 0 \\ -1 & if\ \dfrac{L_h}{c_p}C_d < 0 \end{cases}\,. \tag{5}$$

$$\delta_{q_v} = \begin{cases} 1 & if\ -C_d > 0 \\ -1 & if\ -C_d < 0 \end{cases}\,. \tag{6}$$

The introduction of δ_T and δ_{q_v} ensures that the corresponding forcing terms act in the direction of the C_d.

We implement three scalar forcing methods. The first is Fourier forcing for which the forcing term is constructed in the Fourier space as:[22]

$$\hat{f}_\theta(\boldsymbol{k},t) = \epsilon_\theta \frac{\hat{\theta}(\boldsymbol{k},t)}{\sum_{k_f \epsilon_k} \left|\hat{\theta}(\boldsymbol{k}_f,t)\right|^2} \delta_{k,k_f} . \tag{7}$$

$$\epsilon_\theta = \epsilon_{\theta,in} m_\theta \tag{8}$$

Above, $\hat{\theta}(\boldsymbol{k},t)$ is the Fourier-transformed scalar field and θ is a placeholder for any scalar. The $\epsilon_{\theta,in}$ is the dissipation rate in the initial scalar field and m_θ is a multiplication factor. The forcing wavenumber range is $1 \leq k_f/k_{min} \leq 4.12$, where k_f is the forced wavenumber and $k_{min} = 2\pi/L = 12.27$ is the minimum wavenumber using domain length $L = 0.512\ m$. The second method is mean gradient forcing for which the forcing term is defined in the physical space as:[9]

$$F_{\theta,MG} = w\beta \tag{9}$$

where w is the instantaneous z-velocity and β is the mean scalar gradient. The unit of β is for K/m for temperature forcing and g/kgm for vapor forcing. The β is calculated by matching $F_{\theta,MG}$ with $\hat{f}_\theta^{-1}(\boldsymbol{k},t)$ as:

$$\beta = \langle \frac{\hat{f}_\theta^{-1}(\boldsymbol{k},t)}{w} \rangle \tag{10}$$

Note that $\hat{f}_\theta^{-1}(\boldsymbol{k},t)$ is found by transforming $\hat{f}_\theta(\boldsymbol{k},t)$ back to the physical space. The third method is linear scalar forcing and the forcing term is constructed in the physical space as:[15]

$$F_{\Theta,LN} = \frac{1}{2}\frac{\langle \chi(\Theta) \rangle}{\sigma_\Theta^2}\Theta \tag{11}$$

The rescaled scalar field Θ is defined as[15]

$$\Theta = \theta \sqrt{\frac{\alpha}{\sigma_\theta^2}} \tag{12}$$

where α is the imposed scalar variance. The quantity $\chi(\Theta)$ is the dissipation rate of Θ and is defined as[15]

$$\chi(\Theta) = \frac{\partial \sigma_\Theta^2}{\partial t} \tag{13}$$

We find the α as follows:

$$\hat{f}_\Theta^{-1}(\boldsymbol{k},t) = \frac{1}{2}\frac{\langle \chi(\Theta) \rangle}{\sigma_\Theta^2}\Theta = \frac{1}{2}\frac{\langle \chi(\Theta) \rangle}{\sigma_\Theta^2}\theta \sqrt{\frac{\alpha}{\sigma_\theta^2}}$$

$$\alpha = \left(\frac{2\hat{f}_\Theta^{-1}(\boldsymbol{k},t)}{\langle \chi(\Theta) \rangle} \frac{\sigma_\Theta^2}{\theta} \right)^2 \sigma_\theta^2 \tag{14}$$

Note that the α is updated at every grid point and every timestep, whereas the β is constant in space and updated at every timestep. The β and the α could not be specified a priori in our model unlike in Refs. 9 and 15 because we have two scalar fields with different mean values. Hence, the mean gradient and linear forcing functions are matched with the Fourier forcing function.

We solve the combined (mean plus fluctuating) scalar fields as shown in Eqs. (3) and (4). Since forcing affects both the fluctuating and mean scalar fields, we define scalar forcing functions in a way that avoids unphysical results. For example, a multiplication factor is used in Eq. (8) so that Fourier forcing is neither too weak nor too strong. It is expected that the mean supersaturation decreases and increases to zero (saturation level) during condensation and evaporation, respectively. We find that a strong forcing can cause the mean supersaturation to be less or greater than zero. On the other hand, a weak forcing cannot sustain scalar fluctuations at a desired level. The multiplication factor for temperature (m_T) is larger than that for vapor mixing ratio (m_{q_v}) because the mean temperature is larger than the mean vapor mixing ratio (Table III). Also, the scalar forcing term (F_T or F_{q_v}) interact with the latent heat term. If the former is larger than the latter and they have opposite signs, condensation might take place instead of evaporation and the vice versa, altering the physics of the problem. The delta functions (Eqs. (5) and (6)) confirm that the F_T or F_{q_v} and the C_d have the same sign. In that case, the δ_T and δ_{q_v} augment the changes in the mean temperature and vapor mixing ratio, respectively. Such enhancement of the temperature and vapor mixing ratio gradients is observed in real clouds in response to radiative heating, updrafts, and downdrafts.[23]

C. Growth of cloud droplets and aerosol particles

In the atmosphere, mutual conversion of aerosol particles and cloud droplets takes place. When the environment is supersaturated, aerosol particles condense, grow beyond the critical radii, and activate into cloud droplets. On the contrary, cloud droplets evaporate, shrink below the critical radii, and deactivate into aerosol particles in a subsaturated environment. The critical radius criterion distinguishes between aerosol particles and cloud droplets in our model.[6] To account for curvature and solute effects, we apply the kappa-Kohler theory[24] which defines the particle equilibrium supersaturation S_k as

$$S_k = \frac{A}{r} - \frac{\kappa r_d^3}{r^3 - r_d^3(1-\kappa)}. \tag{15}$$

where r_d is the dry aerosol radius, r is the particle (wet) radius, and κ is the hygroscopicity of the solute. Parameter A is defined as:[6]

$$A = \frac{2\sigma_l M_l}{RT\rho_l}. \tag{16}$$

The critical radius (r_c) and critical equilibrium supersaturation (S_c) can be found as:[25]

$$r_c = \sqrt{\frac{3\kappa r_d^3}{A}}, \qquad S_c = \frac{2}{\sqrt{\kappa}}\left(\frac{A}{3r_d}\right)^{\frac{3}{2}}. \tag{17}$$

The motion of each aerosol particle or cloud droplet is represented in the Lagrangian fashion, which consists of the kinematics and the Newton's law. The simplified equations used for the Lagrangian position and velocity can be written as[5]

$$\frac{d\boldsymbol{X}_i(t)}{dt} = \boldsymbol{V}_i(t), \tag{18}$$

$$\frac{d\boldsymbol{V}_i(t)}{dt} = \frac{1}{(\tau_p)_i}[\boldsymbol{u}_i(\boldsymbol{X},t) - \boldsymbol{V}_i(t)] + \boldsymbol{g}. \tag{19}$$

where the subscript 'i' denotes the i-th aerosol particle or cloud droplet, $\boldsymbol{V}$ is its velocity vector, and $\boldsymbol{X}$ is its position vector. $\boldsymbol{u}_i$ is the instantaneous fluid velocity vector at the position of particle i and is obtained through a trilinear interpolation of the Eulerian field. The particle response time τ_p is given by[5]

$$(\tau_p)_i = \frac{2\rho_l r_i^2}{9\rho_a \nu}. \tag{20}$$

The change in particle (aerosol or cloud) radius during condensation (or evaporation) is described by[26]

$$\frac{dr_i(t)}{dt} = \frac{G}{r_i(t)}\left(S_e(\boldsymbol{X},t) - S_k(\boldsymbol{X},t)\right)_i. \tag{21}$$

where S_e is the environmental supersaturation and is related to q_v and T by

$$S_e = \frac{q_v}{q_{v,s}} - 1, \tag{22}$$

where $q_{v,s}$ is the saturation water vapor mixing ratio.[27] The S_e is a Eulerian quantity in Eq. (22) but interpolated to the particle position in Eq. (21). The growth parameter G is expressed as[26]

$$G = \frac{1}{\frac{L_h\rho_l}{k_T'T}\left(\frac{L_h}{R_vT} - 1\right)(1 + S_k) + \frac{\rho_l R_v T}{\mu_v' p_{sat}}}, \tag{23}$$

where k_T' and μ_v' are the modified thermal conductivity and modified water vapor diffusivity,[28] respectively. With the foregoing, the C_d is determined as:[5]

$$C_d(\boldsymbol{x},t)=\frac{4\pi\rho_l G}{\rho_a a^3}\sum_{i=1}^{n} r_i(t)\big(S_e(\boldsymbol{X},t)-S_k(\boldsymbol{X},t)\big)_i\,. \tag{24}$$

where n is the number of particles in a grid cell that has a volume of a^3.

III. NUMERICAL DETAILS

We conduct two studies: Study I and Study II. The first is for condensation and activation of aerosol particles into cloud droplets, while the second is for evaporation and deactivation of cloud droplets into aerosol particles. Note that condensation and evaporation occur in different physical locations of a cloud that are exposed to humid air and dry air, respectively.[6]

A. The numerical model

By varying the range of forced wavenumbers,[6] we generate two turbulence levels: 'low' and 'high', and denote them as 'L' and 'H', respectively. Specifically, we apply forcing in the wavenumber bands: $1 \le k_f/k_{min} \le 4.12$ and $1 \le k_f/k_{min} \le 12.12$, respectively. The number of grid points N is 256 in one coordinate direction and the domain length L is 0.512 m. Note that the maximum wavenumber $k_{max}{\sim}128k_{min}$ in our model. The initial TKE spectrum is identical for both turbulence levels and is specified as[29]

$$E(k)=\frac{16}{\sqrt{\pi/2}}\frac{u_0^2k^4}{k_0^5}\exp\left(-\frac{2k^2}{k_0^2}\right). \tag{25}$$

where $k_0=4.12k_{min}$ and $u_0=0.16\ m/s$ is the root-mean-square (rms) velocity.

Table I lists the statistics of turbulent velocity field such as the turbulent kinetic energy, $\hbar$, its dissipation rate, ϵ, the rms velocity, u_{rms}, the Kolmogorov length scale η, the Taylor micro-scale, λ, the length scale characterizing large eddies, l_0, the forcing Reynolds number, Re_f, the Taylor-scale Reynolds number, Re_λ, and the Reynolds number based on l_0, Re_{l_0}. The abovementioned quantities have been defined in Ref. 6. The integral length scales (l), calculated as shown in Ref. 6, are 0.14 m and 0.08 m for 'low' and 'high' turbulence levels, respectively. The parameter ranges listed in Table I are representative of cloud turbulence.[30]

Table I. Statistics of the velocity fields at 4 s

Turbulence level	$\hbar$ (m^2/s^2)	ϵ (m^2/s^3)	u_{rms} (m/s)	λ (m)	η (m)	l_0 (m)	Re_f	Re_λ	Re_{l_0}
High	0.0094	0.00494	0.1386	0.0169	0.00091	0.184	401.12	156.11	1704.7
Low	0.0025	0.00055	0.0797	0.0261	0.00157	0.227	192.97	138.74	1207.6

The physical model simulated is that of a cubic domain (box) inside which turbulence, cloud droplets, and aerosol particles interact. The boundary conditions are triply periodic, and the domain volume is $0.512^3\ m^3$. At the start of simulations, the domain is divided equally into cloudy and clear-air regions. Cloud droplets or aerosol particles are placed in the cloudy region initially and subsequent turbulent mixing causes them to spread to all over the domain. A slab-like cloud configuration (Fig. 1) is assumed for the initial field,[6] to enable a sharp transition in the water vapor mixing ratio and temperature at the cloud-clear air interface.

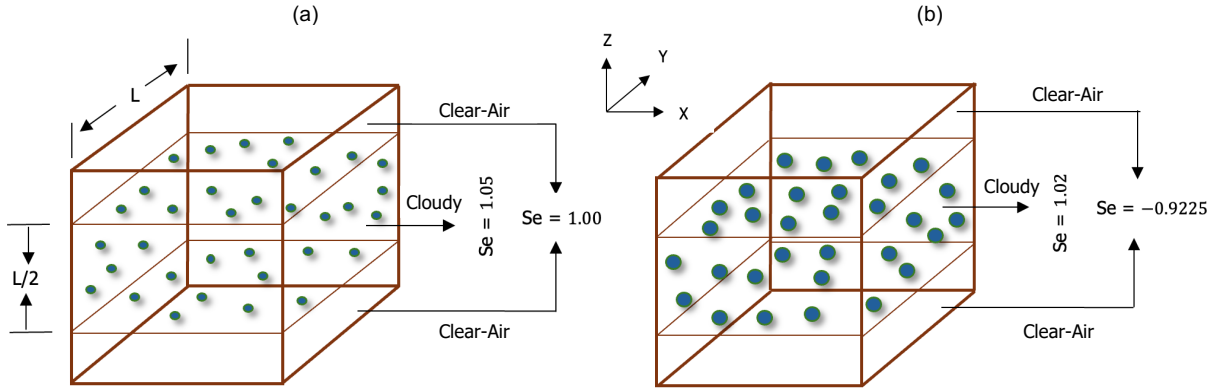

FIG. 1 Initial configurations for (a) Study I, and (b) Study II. The middle half represents the cloudy region while the top and bottom one-fourths constitute the clear-air region. The cloudy region is initially 5% supersaturated in Study I and 2% in Study II. The clear-air region is just saturated in the first and -92.25% subsaturated in the second. The spheres represent aerosol particles in Study I and cloud droplets in Study II.

In Study I, the cloudy region is supersaturated (humid), but the clear-air region is just saturated at initial time. The initial vapor mixing ratio field is specified as:[6]

$$q_v(z, t=0) = \begin{cases} q_v^{max}, & d - L \times 0.5 \times 0.5 \le z < d + L \times 0.5 \times 0.5 \\ q_{v,e}, & elsewhere \end{cases}. \tag{26}$$

The value of $q_{v,s}$ in Eq. (22) is $3.872\ g/kg$. Above, $q_v^{max} = 1.05 \times q_{v,s} = 4.066\ g/kg$, and $q_{v,e} = 3.872\ g/kg$. The length, $d \equiv L/2$ is the width of the cloud slab. To resolve the discontinuous distribution (Eq. (26)), we choose a DNS model based on finite difference[6] instead of a pseudospectral DNS model because the latter could give rise to artificial oscillations (Gibbs phenomenon).[31] The temperature field is initialized as:[6]

$$T(t=0) = \langle T(t=0) \rangle - 0.608 \langle T(t=0) \rangle (q_v(z, t=0) - \langle q_v(t=0) \rangle)\,. \tag{27}$$

16×10^6 dry aerosols are randomly placed in the cloudy region at the start of simulations. The number concentration is $119\ cm^{-3}$. We simulate six cases namely L, L-F, L-MGF, L-LF, H, and H-F, which are summarized in Table II. The identifiers 'L' and 'H' before the dash (-) imply 'low' and 'high' flow turbulence levels, respectively. The identifier 'F' after the dash (-) indicate that scalar forcing is applied in the Fourier space while 'MGF' and 'LF' denote

mean scalar gradient forcing and linear forcing, respectively. The β is calculated using Eq. (12) and the α is calculated using Eq. (16). Note that momentum forcing is implemented in the Fourier space for all cases. The size distributions of dry aerosol particles are assumed to be lognormal with geometric mean radius of 0.126 μm and standard deviation of 0.02 μm. The initial volume fraction occupied by dry aerosol particles is approximately 9.98×10^{-11} % and the average Stokes number (S_t) is 7.35×10^{-8}. Dry aerosols (solutes) absorb water from the surrounding to become aqueous aerosol particles which grow and activate into cloud droplets in Study I.

TABLE II. Cases in Study I and Study II. Case L has 'low' turbulence level but without scalar forcing. Case L-F has 'low' turbulence level and scalar forcing is implemented in the Fourier space. Case L-MGF applies mean scalar gradient forcing in the physical space and calculates the β adaptively. Case L-LF implements linear scalar forcing in physical space and calculates the α adaptively. Cases H and H-F are analogous to Cases L and L-F except that the turbulence level is 'high'.

Case	Dry aerosol size (μm)	TKE dissipation rate (m^2/s^3)	Turbulence level	Scalar forcing type	Initial particle size in Study I (μm)	Initial particle size in Study II (μm)
L	0.126 ± 0.02	0.0025	Low	N/A	0.126 ± 0.02	10
L-F	0.126 ± 0.02	0.0025	Low	Fourier	0.126 ± 0.02	10
L-MGF	0.126 ± 0.02	0.0025	Low	Mean gradient	0.126 ± 0.02	10
L-LF	0.126 ± 0.02	0.0025	Low	Linear	0.126 ± 0.02	10
H	0.126 ± 0.02	0.0094	High	N/A	0.126 ± 0.02	10
H-F	0.126 ± 0.02	0.0094	High	Fourier	0.126 ± 0.02	10

In Study II, the cloudy region is supersaturated (humid) but the clear-air region is subsaturated (dry) at the start of simulations. The same configuration for vapor mixing ratio as in Eq. (26) is used except that $q_v^{max} = 1.02 \times q_{v,s} = 3.949\ g/kg$ and $q_{v,e} = 0.30\ g/kg$. The temperature field is initialized as described in Eq. (27). A total of 16×10^6 cloud droplets, having a monodisperse size (radius) distribution of 10 μm, are randomly placed in the cloudy region at the start of simulations. The initial volume fraction occupied by cloud droplets is 4.99×10^{-5} % and the average S_t is 4.63×10^{-4}. Cloud droplets evaporate, shrink in size, and deactivate into aerosol particles in Study II.

Particles are inserted in the domain after 2 s, when the TKE dissipation rates become statistically stationary. The initial dissipation rates in the temperature ($\epsilon_{T,in}$) and vapor mixing ratio ($\epsilon_{q_v,in}$) fields are included in Table III. The Schmidt number ($Sc = \nu/\mu_T$) is 0.68 for both temperature and vapor mixing ratio. The Bachelor length scales ($\eta_B = \eta/\sqrt{Sc}$) are 0.0019 m and 0.0011 m for 'low' and 'high' turbulence intensities, respectively. However, the effective Sc is higher in our model because scalar fields are coupled with particles via latent heat terms. To balance the grid resolution requirement and computational cost, we carry out all the simulations using 256^3 grid points. The $k_{max}\eta$

values for 'low' and 'high' turbulence levels are 2.46 and 1.43, respectively. The FronTier software package[32] is used to solve the governing equations. The details regarding discretization and numerical solution techniques can be found in Ref. 6. We used the Perlmutter supercomputer managed by National Energy Research Scientific Computing Center (NERSC), United States Department of Energy, USA.

B. List of parameters

We list the constants and parameters of our DNS model in Table III. The hygroscopicity parameter (κ) of 0.61 is used to represent ammonium sulfate aerosols.[32]

TABLE III. Parameters with initial values, and other constants

Symbol	Value	Unit	Symbol	Value	Unit
q_v^{max}	4.066 (Study I) 3.949 (Study II)	g/kg	$q_{v,e}$	3.872 (Study I) 0.30 (Study II)	g/kg
L_h	2.5×10^6	J/kg	c_p	1005.0	J/kg/K
ρ_a	1.0	kg/m^3	ν	1.5×10^{-5}	m^2/s
ρ_l	1000	kg/m^3	p	82844.14	N/m^2
$\langle T(t=0)\rangle$	270.75	K	R_v	461.5	J/kg/K
k_T	0.0238	W/m/K	σ_l	0.072	N/m
$\mu_T = \mu_v$	2.16×10^{-5}	m^2/s	M_l	0.018	kg/mol
R	8.314	J/mol/K	S_t	7.35×10^{-8} (Study I) 4.63×10^{-4} (Study II)	-
κ	0.61	-			
$\epsilon_{T,in}$	2.16×10^{-5} (Study I) 7.7×10^{-3} (Study II)	K^2/s	$\epsilon_{q_v,in}$	7.9×10^{-4} (Study I) 2.8×10^{-1} (Study II)	(g/kg)^2/s
m_T	10 (Study I) 1 (Study II)	-	m_{q_v}	0.1 (Study I) 0.1 (Study II)	-

C. Model validation

We ran our model using the parameters of Overholt and Pope[9] who applied mean scalar gradient forcing. The time evolution of normalized scalar variance is plotted in Fig. 2(a). The Cases OP-1996 and OP-128 in Fig. 2(a) represent Overholt and Pope[9] (Run 128.3) and our run, respectively. The number of grid points is 128^3 for both cases. The variance of the scalar field σ_θ^2 is:

$$\sigma_\theta^2 = \frac{\sum_i (\theta_i - \bar{\theta})^2}{N}. \tag{28}$$

where N is the number of grid points. The variance is zero initially for both cases and no latent heat term is present in the scalar transport equation. The scalar variance is normalized by $(\beta L_\epsilon)^2$, where L_ϵ is a turbulent length scale.[9] The fluctuating scalar field is normalized by its standard deviation σ_θ, and the normalized time is t/T_E, where t is the physical simulation time and T_E is the eddy turnover time.[9] We find that the normalized scalar variances for Cases OP-1996 and OP-128 (Fig. 2(a)) are almost equal once they become statistically stationary (t/T_E~6). The differences between them from 2 to 6 (abscissa) can be attributed to the transient behavior in respective models.

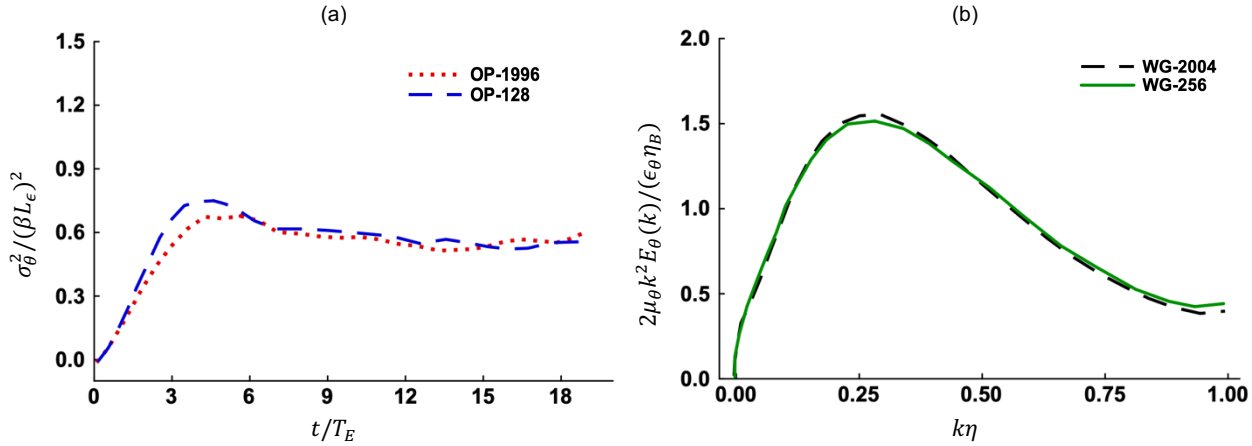

FIG. 2 Comparison of (a) normalized scalar variances and (b) normalized scalar dissipation spectra.

We also validate our model against that of Watanabe and Gotoh[13] who carried out scalar forcing in the Fourier space. According to Ref. 13, the normalized scalar dissipation spectrum is: $2\mu_\theta k^2 E_\theta(k)/(\epsilon_\theta \eta_B)$, where μ_θ, E_θ, and ϵ_θ are diffusivity, spectrum, and dissipation rate in the scalar field θ, respectively. Figure 2(b) shows the normalized scalar dissipation spectra for Cases WG-2004 and WG-256 which represent Watanabe and Gotoh[13] (Run 1) and our run, respectively. The number of grid points is 512^3 for the former but 256^3 for the latter. We find excellent agreement between the two profiles in Fig. 2(b).

IV. RESULTS AND DISCUSSIONS

The results from our simulations are presented in this section. We discuss the impact of scalar forcing on the fluctuating and mean scalar fields during condensation and evaporation. Then we evaluate the role of scalar forcing on activation and deactivation processes. The effects of flow turbulence intensity on scalar fluctuations and cloud microphysics are also discussed.

A. The impact of forcing on fluctuating and mean scalar fields

1. Condensation (Activation)

Study I is concerned with condensational growth and aerosol activation. The temporal changes of the variances of fluctuating temperature (σ_T^2), vapor mixing ratio ($\sigma_{q_v}^2$), and environmental supersaturation ($\sigma_{S_e}^2$) are shown in Figs. 3(a)-(c), respectively. We see that the magnitudes of scalar fluctuations are nonzero initially. The forced scalar fields attain statistical stationarity but the unforced scalar fields in Case L continue to decay. The magnitudes of fluctuations are largest for Case L-MGF but very close for Cases L-F and L-LF. The mean gradient forcing term, unlike the linear forcing term, is not matched with the Fourier forcing term at every nodal point. Rather, the mean gradient β is found by spatial averaging (Eq. (10)). In absence of forcing, the fluctuating scalar fields decay due to mixing between the cloudy and clear-air regions. Whereas scalar forcing acts as a source of fluctuations and counteracts the decay.

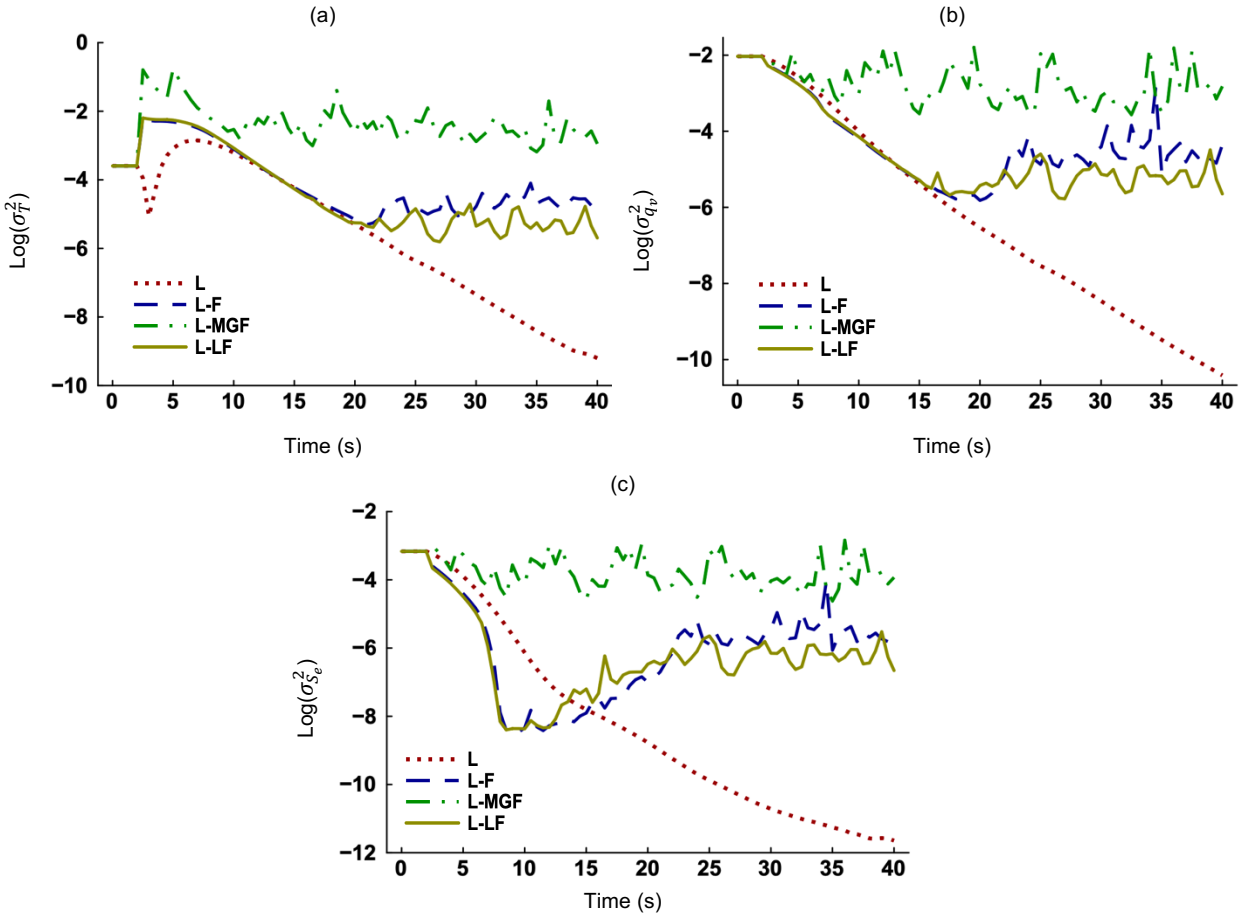

FIG. 3 Time evolution of the variances of (a) fluctuating temperature, (b) fluctuating vapor mixing ratio, and (c) fluctuating environmental supersaturation, in Study I. Scalar forcing is absent in Case L. Case L-F implements scalar forcing in the Fourier space. Case L-MGF applies mean scalar gradient forcing and calculates the β adaptively. Case L-LF has linear scalar forcing and calculates the α adaptively. The turbulence level is 'low' for all cases.

The spectra[33] of the fluctuating temperature and vapor mixing ratio are plotted in Figs. 4(a)-(b). They show the distribution of scalar fluctuations across scales. According to the Kolmogorov's theory, small-scale structures should be universal and independent of the large-scale anisotropy.[34] However, small-scale universality is not observed in the scalar fields when forcing is applied. We see that the spectra for Cases L and L-F differ at the intermediate and small scales while those for Cases L and L-MGF differ at all scales. A flat region ($3.0 \leq \log(k) \leq 3.2$) can be identified in the spectra for Case L, which suggests the existence of a viscous-convective regime, typically observed for scalars with Schmidt number (Sc) greater than unity.[35] The Sc for both scalars are less than unity (0.68) in our model without consideration of particles. But the coupling of scalar fields with tiny cloud droplets and aerosol particles correspond to $Sc > 1$ as transport of mass (particles) is slower than transport of momentum. The flat region expands further ($1.8 \leq \log(k) \leq 3.2$) for Cases L-F and L-LF, and the viscous convective regime appears to suppress the inertial convective regime for these two forced cases. Consequently, the spectral slopes deviate from the -5/3 law in the inertial convective regime as seen in Figs. 4(a)-(b). A key feature of higher Sc is the increase of high-wavenumber contribution to the scalar spectrum.[36] We observe that fluctuations increase at the intermediate and small scales for Cases L-F and L-LF compared to the unforced case (L). When mean gradient forcing is applied at physical-space nodal points (Case L-MGF), fluctuations increase at all scales compared to Case L. The area under the curve is also largest for Case L-MGF (Figs. 4(a)-(b)).

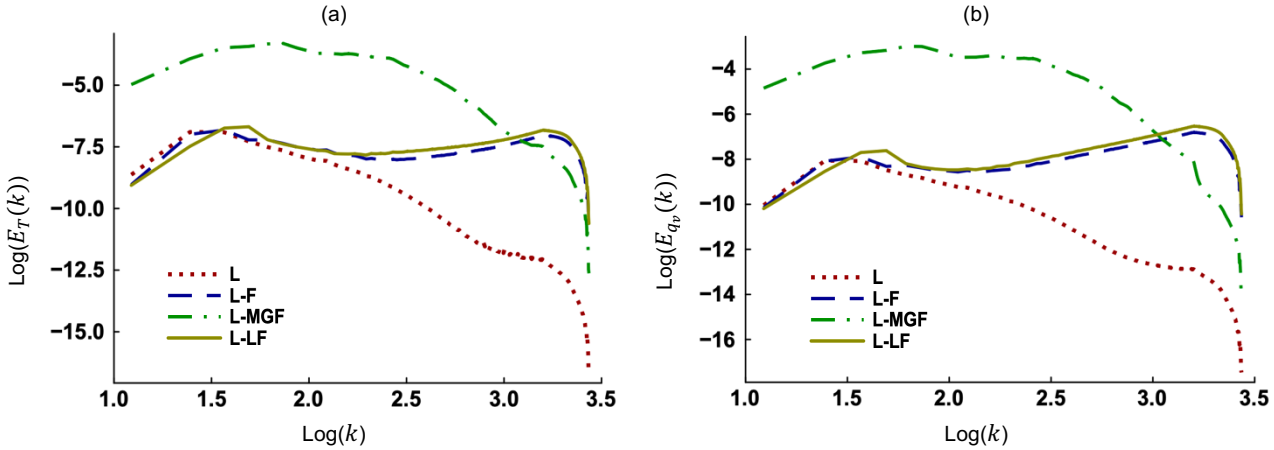

FIG. 4 Log-log spectra of the fluctuating (a) temperature and (b) vapor mixing ratio fields, in Study I at 25 s.

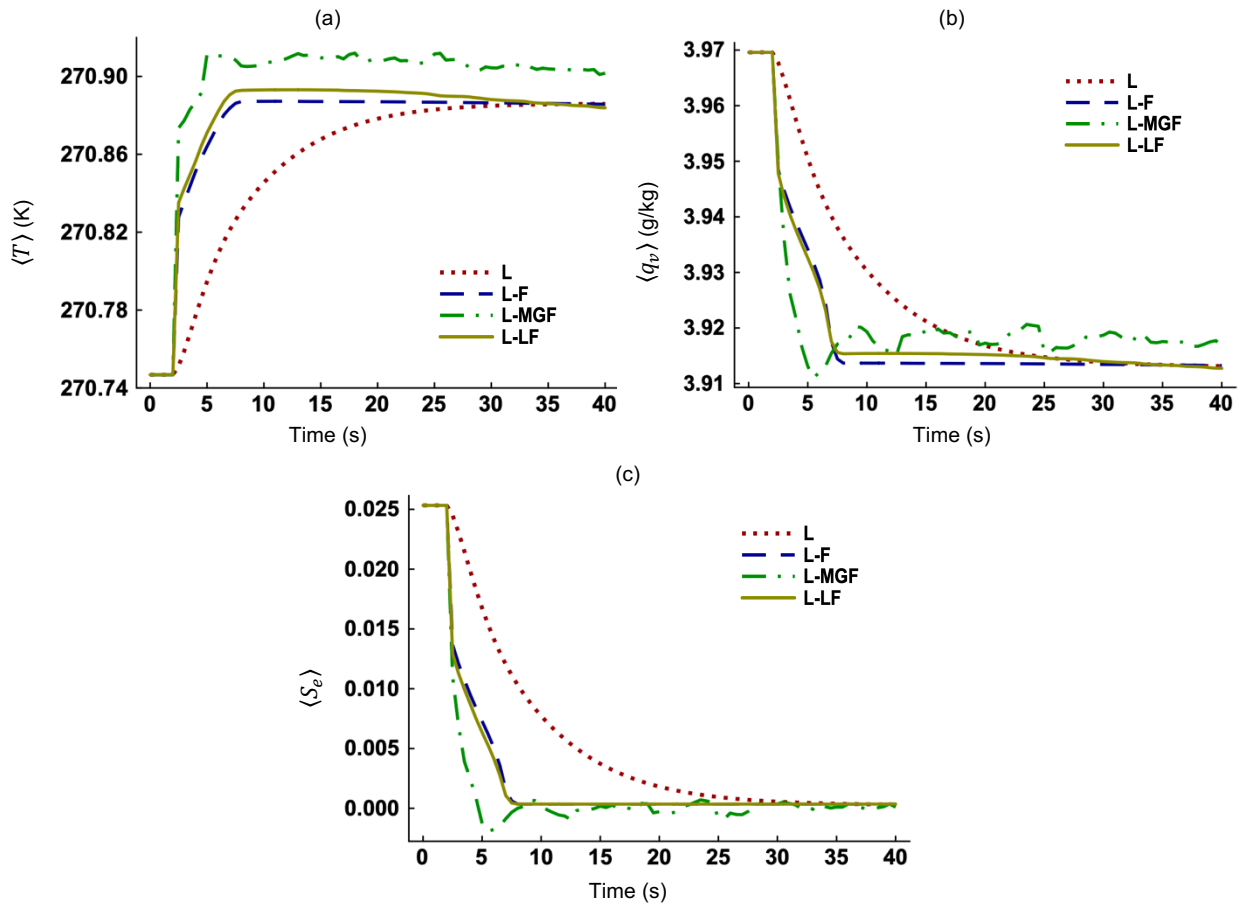

FIG. 5 Time evolution of (a) mean temperature ($\langle T \rangle$), (b) mean vapor mixing ratio ($\langle q_v \rangle$), and (c) mean environmental supersaturation ($\langle S_e \rangle$), in Study I. Scalar forcing is absent in Case L. Case L-F implements scalar forcing in the Fourier space. Case L-MGF applies mean scalar gradient forcing and Case L-LF has linear scalar forcing. The turbulence level is 'low' for all cases.

Figures 5(a)-(c) show the temporal evolution of mean scalar fields in Study I. The time rates of increase in the $\langle T \rangle$ and decrease in the $\langle q_v \rangle$ and $\langle S_e \rangle$ are slowest when scalar forcing is absent (Case L). Conversion of water vapor into liquid water during condensation decreases the $\langle q_v \rangle$ and thus the $\langle S_e \rangle$. Figure 5(c) shows that the system reaches equilibrium (no further growth or decay of particles) by approximately 35 s for Case L and 7 s for the forced cases. Forcing causes the mean scalar fields to relax to their equilibrium states faster because it acts in the direction of phase change. Equilibrium corresponds to saturation ($\langle S_e \rangle \sim 0$) for all cases.

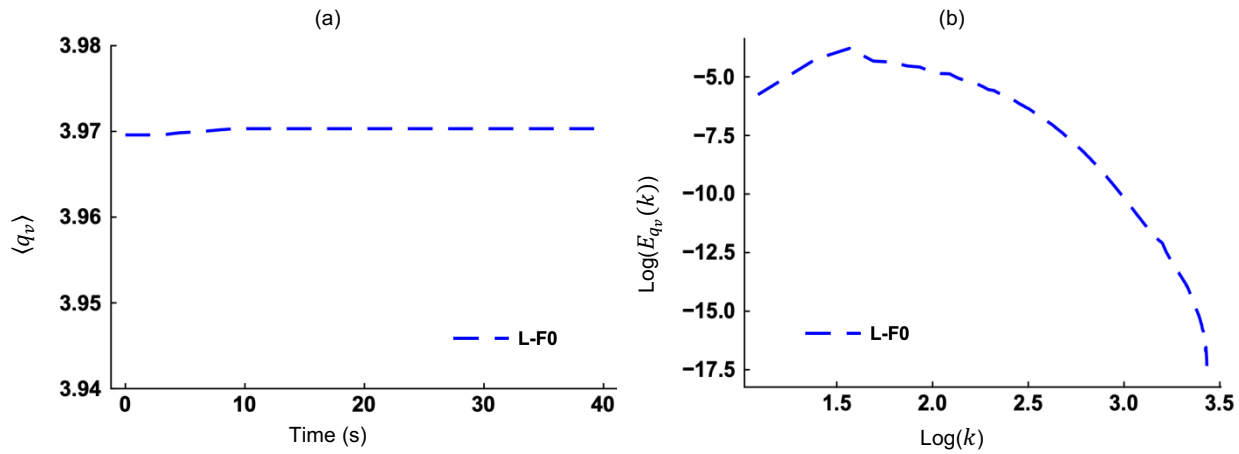

FIG. 6 (a) Time evolution of the mean vapor mixing ratio ($\langle q_v \rangle$) and (b) Log-log spectrum of the fluctuating vapor mixing ratio (q_v') at 10 s, for Case L-F0 in Study I. Case L-F0 is Case L-F except that particle radius is set to zero.

To recognize the effects of particles on scalar fields, we simulate Case L-F0 by setting particle size (r) to zero. When the r is zero, the C_d is zero (Eq. (26)) and the latent heat terms in Eqs. (3) and (4) are zero. Figure 6(a) shows the time evolution of the $\langle q_v \rangle$ and Fig. 6(b) plots the $E_{q_v}(k)$ at 10 s. We see that the temporal variation in the $\langle q_v \rangle$ is negligible for Case L-F0. Exclusion of particles prevents the mutual conversion of water vapor and liquid water. So, the $\langle q_v \rangle$ remains constant as phase change cannot take place. The $E_{q_v}(k)$ decays from its peak at $\log(k) \sim 1.5$ (Fig. 6(b)) and conforms to the turbulence theory[2] when Fourier forcing is applied but particles are absent (Case L-F0). Thus, forcing itself does not cause deviation from homogeneity and isotropy in the scalar fields.

2. Evaporation (Deactivation)

Study II focuses on evaporation and deactivation of cloud droplets. The temporal evolution of the relative dispersions of the scalar fields ($\sigma_\theta / \langle \theta \rangle$) in Study II is plotted in Figs. 7(a)-(c). While the scalar fields decay in absence of forcing, the forced scalar fields become statistically stationary. In actual clouds, the magnitudes of fluctuations in the temperature and vapor mixing ratio are much smaller than the mean,[37] which is also the case in our study. The $\sigma_T / \langle T \rangle$ and $\sigma_{q_v} / \langle q_v \rangle$ for Case L in Study II at 25 s are $1.6e-5$ and $2.97e-3$, respectively. The corresponding ratios for Case L-F are $8.5e-5$ and $2.73e-2$, respectively. So, fluctuations in the temperature and vapor mixing ratio increase with forcing but the standard deviations remain smaller than the means. The ratio $\sigma_{S_e} / \langle S_e \rangle$ is $8.78e-3$ for Case L but 9.04 for Case L-F in Study II at 25 s. Hence, the σ_{S_e} is larger than the $\langle S_e \rangle$) for Case L-F while the opposite is true for the unforced case (L). This finding is consistent with the model of Paoli et al.[16] that applied scalar forcing

in the Fourier space. Because the $\langle S_e \rangle$ is much smaller than the $\langle T \rangle$ and $\langle q_v \rangle$, fluctuations in the supersaturation are more pronounced with forcing. Note that the σ_{S_e} often exceed the $\langle S_e \rangle$ in atmospheric clouds.[38]

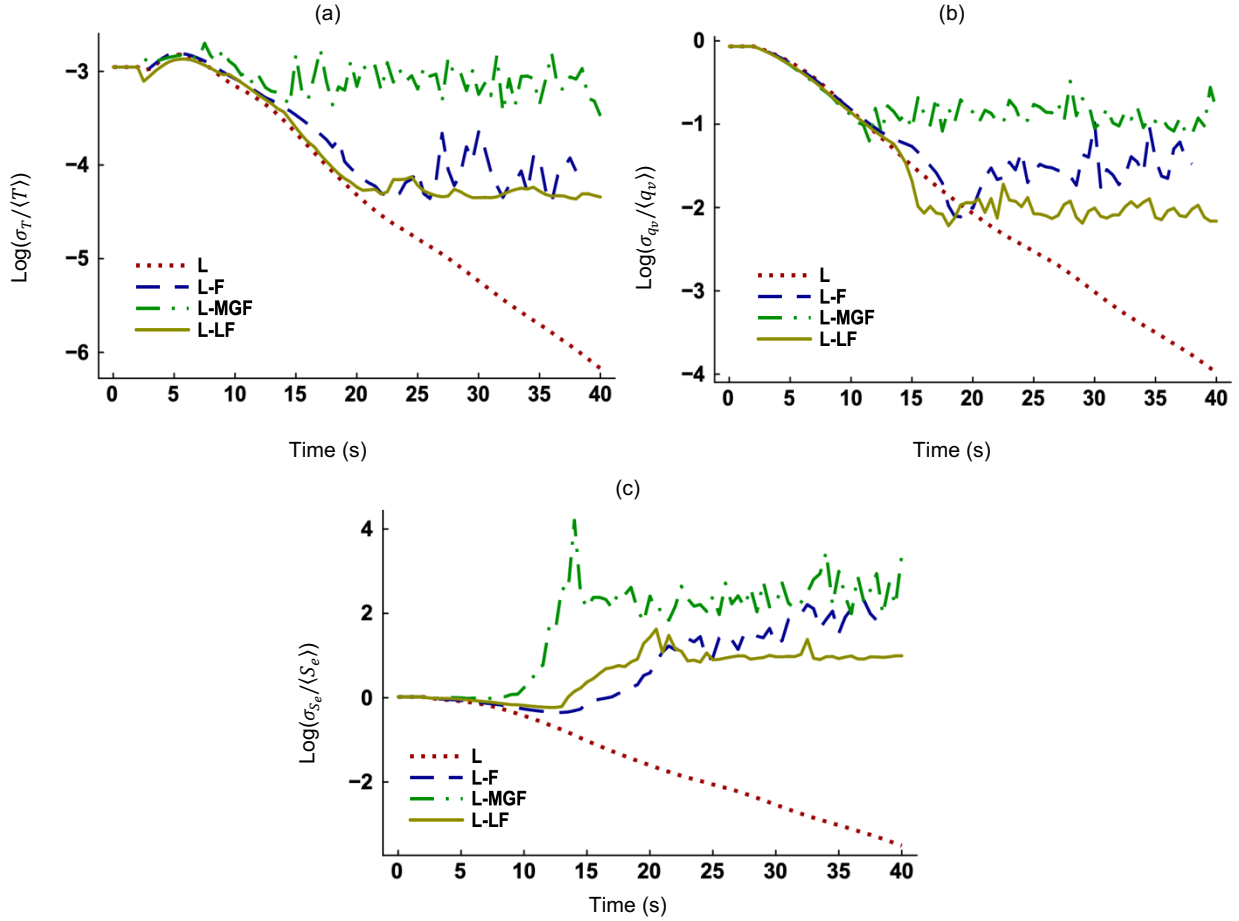

FIG. 7 Time evolution of the relative dispersions of (a) temperature, (b) vapor mixing ratio, and (c) environmental supersaturation, in Study II. Scalar forcing is absent in Case L. Case L-F implements scalar forcing in the Fourier space. Case L-MGF applies mean gradient forcing and Case L-LF has linear forcing. The turbulence level is 'low' for all cases.

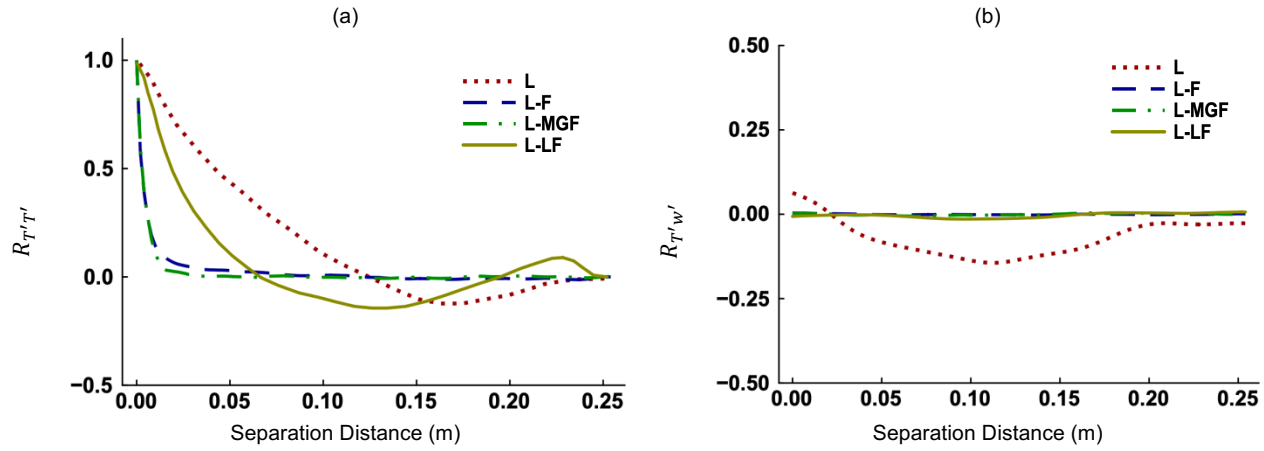

FIG. 8 The correlation coefficients (a) $R_{T'T'}$ and (b) $R_{T'w'}$ in Study II at 25 s.

Spatial correlation coefficient quantifies the mutual dependence between two quantities separated in space. The autocorrelation coefficient $R_{T'T'}$ is defined as[33]

$$R_{T'T'}(\boldsymbol{r}) = \frac{\langle T'(\boldsymbol{x},t)T'(\boldsymbol{x}+\boldsymbol{r},t)\rangle}{\sqrt{\langle\left(T'(\boldsymbol{x},t)\right)^2\rangle\langle\left(T'(\boldsymbol{x},t)\right)^2\rangle}}, \qquad \boldsymbol{r} = \Delta x\boldsymbol{i} + \Delta y\boldsymbol{j} + \Delta z\boldsymbol{k}\,. \tag{29}$$

where $\boldsymbol{r}$ is the separation distance vector and T' is the fluctuating environmental supersaturation. Similarly, the cross-correlation coefficient $R_{T'w'}$ can be defined where w' is the fluctuating z-velocity. The $R_{T'T'}$ and $R_{T'w'}$ are plotted in Figs. 8(a)-(b), respectively. As separation distance increases, the $R_{T'T'}$ decays more quickly for Cases L-F, L-MGF, and L-LF compared to the unforced case (L). Rapid decorrelation suggests that turbulent structures cannot maintain coherence over a long distance. This happens when fluctuations in the scalar fields are driven by external forcing. We also see in Fig. 8(b) that the $R_{T'w'}$ is essentially zero and thus the T' and w' are not correlated at all for the forced cases. This confirms that fluctuations in the forced scalar fields are not driven by flow turbulence.

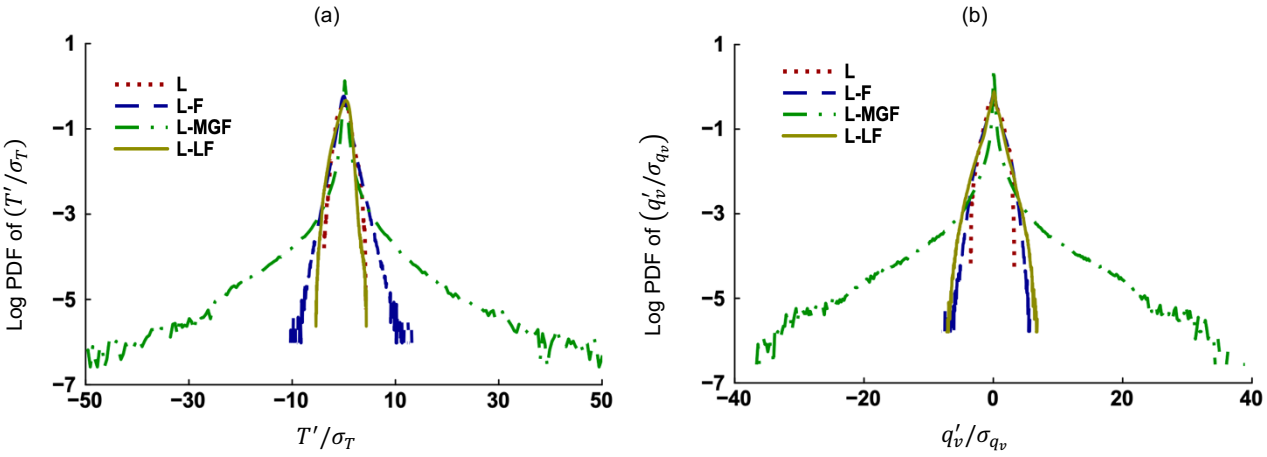

FIG. 9 Log PDFs of the (a) fluctuating temperature (T') normalized by its standard deviation (σ_T), and (b) fluctuating vapor mixing ratio (q_v') normalized by its standard deviation (σ_{q_v}), at 25 s in Study II.

Figure 9(a) shows the PDFs of T'/σ_T, which is the fluctuating temperature normalized by standard deviation, at 25 s for the four cases. Figure 9(b) is analogous to Fig. 9(a) but for vapor mixing ratio. It appears that the normalized PDFs in both figures are broader for Case L-MGF compared to the other cases. To assess how much Gaussian or non-Gaussian the distributions are, we calculate their skewness (γ) and kurtosis (ω) as[34]

$$\gamma = \frac{\langle(\varphi')^3\rangle}{\langle(\varphi')^2\rangle^{3/2}}, \quad \omega = \frac{\langle(\varphi')^4\rangle}{\langle(\varphi')^2\rangle^{4/2}}, \quad \varphi = \frac{\theta'}{\sigma_\theta}. \tag{30}$$

The γ of temperature PDFs in Fig. 9(a) are 0.055, 0.28, -0.12, and -0.76 for Cases L, L-F, L-MGF, and L-LF, respectively, while the corresponding ω are 3.21, 6.68, 425.2, and 3.73. The γ of vapor PDFs in Fig. 9(b) are 0.09,

0.003, -0.035, and -0.31, respectively, while the corresponding ω are 3.03, 4.43, 176.2, and 5.84. Note that skewness is 0 and kurtosis is 3 for a perfectly Gaussian distribution. The kurtosis for Case L in both figures are close to 3 but are larger than 3 for the forced cases. So, forcing makes the PDFs of fluctuating scalar fields non-Gaussian. Previous studies of cloud turbulence found that thermodynamic fluctuations can be both Gaussian and non-Gaussian.[39,40] With mean gradient forcing (Case L-MGF), the PDFs in Figs. 9(a)-(b) have heavy tails and their kurtosis are very high. Hence, extreme values are observed for this case although most values are closer to the mean. Physically, extreme temperature and vapor fluctuations signify that mixing between cloud and surrounding air is intense.[41]

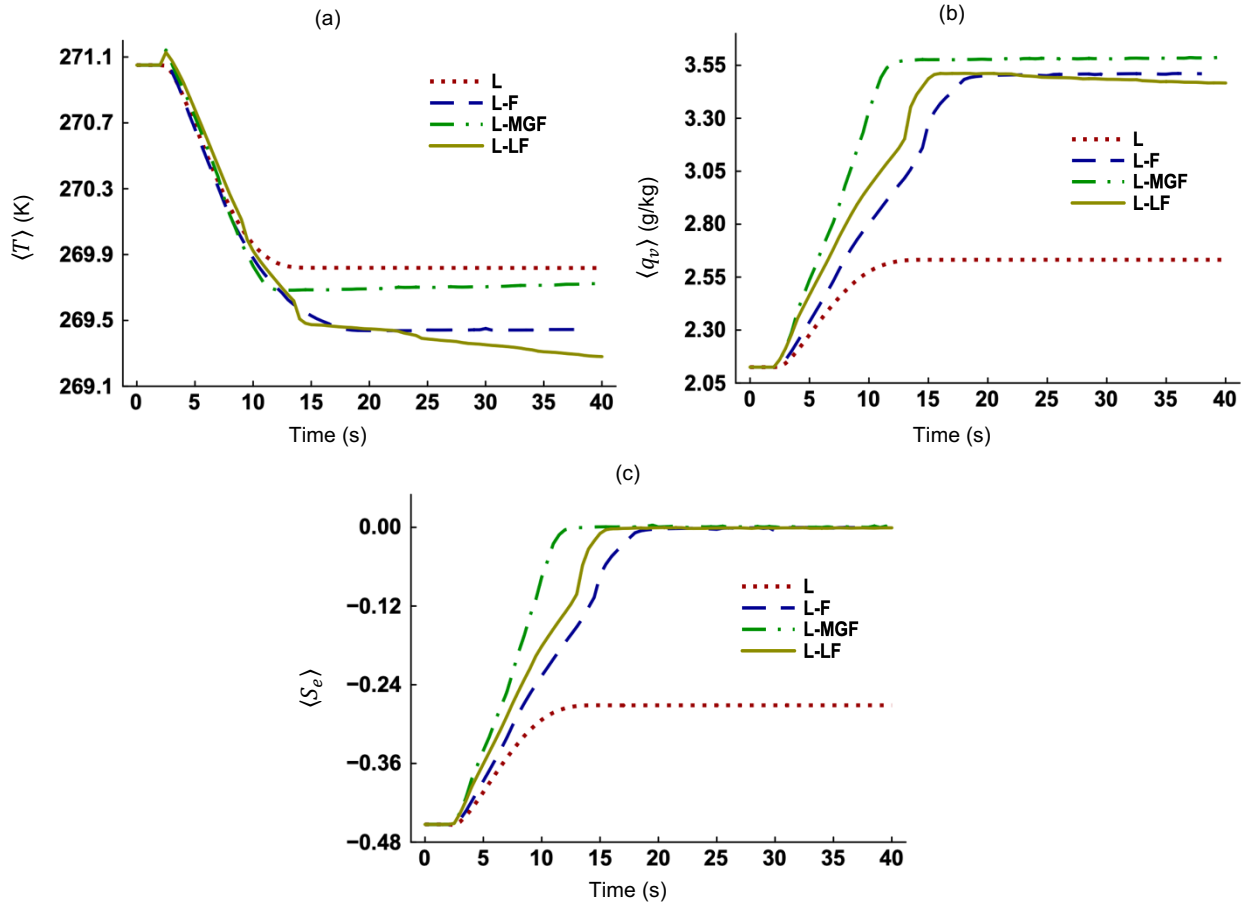

FIG. 10 Time evolution of (a) mean temperature ($\langle T \rangle$), (b) mean vapor mixing ratio ($\langle q_v \rangle$), and (c) mean environmental supersaturation ($\langle S_e \rangle$), in Study II. Scalar forcing is absent in Case L. Case L-F implements scalar forcing in the Fourier space. Case L-MGF applies mean scalar gradient forcing and Case L-LF has linear scalar forcing. The turbulence level is 'low' for all cases.

The temporal evolution of the mean scalar fields for Study II is shown in Figs. 10(a)-(c). We see that the growth and decay profiles are opposite to those in Figs. 6(a)-(c). During evaporation, liquid water converts into water vapor, increasing the $\langle q_v \rangle$ and $\langle S_e \rangle$. The decrease in $\langle T \rangle$ is a manifestation of evaporative cooling. Equilibrium is reached before saturation ($\langle S_e \rangle \sim 0$) for Case L (Fig. 10(c)). Absence of scalar forcing (Case L) leads to faster evaporation and

the profile of $\langle S_e \rangle$ settles to an asymptote when all droplets evaporate fully. On the other hand, equilibrium corresponds to saturation for the forced cases and is reached before evaporation is complete.

B. The impact of scalar forcing on cloud microphysics

1. Activation of aerosol particles

To recognize the impact of scalar forcing on condensation (activation), we plot the fraction of aerosol particles that activate into cloud droplets with time in Fig. 11(a). The activation process is very fast between 2 s to 5 s for Case L and slows down afterwards. For the forced cases, the activation fraction is lower because equilibrium is reached before aerosol particles could grow sufficiently to be activated. Interestingly, the activation profile for Case L-MGF decreases slightly after its peak at around 4 s. Thus, a small number of particles deactivate after activation for this case due to negative fluctuation. Figure 11(b) show the time evolutions of the mean radius. The profiles tend to asymptote after exponential increase at early times. For the unforced case (L), particle growth (Fig. 11(b)) and activation fraction (Fig. 11(a)) are highest. Scalar forcing drives the system towards equilibrium faster (Figs. 5 and 10). That leaves less time available for completion of phase change.[42] Hence, particle growth (condensation) is reduced, and activation is suppressed.

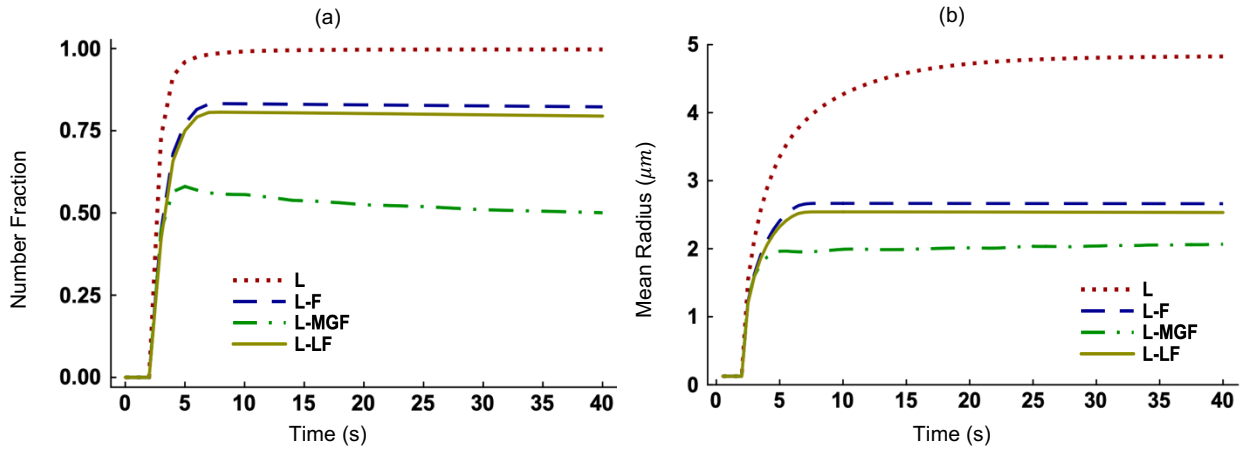

FIG. 11 Time evolution of the (a) number fraction of activated aerosol particles, and (b) mean radius of all particles, in Study I. Scalar forcing is absent in Case L. Case L-F implements scalar forcing in the Fourier space. Case L-MGF applies mean scalar gradient forcing and Case L-LF has linear scalar forcing. The turbulence level is 'low' for all cases.

Fluctuations in the S_e have impact on activation and deactivation. Based on Eq. (21), particle growth is positive if $S_e > S_k$ and negative when $S_e < S_k$. Positive growth means condensation and potential activation while negative growth means evaporation and potential deactivation. Figures 12(a)-(b) show the PDFs of S_e and S_k for Case L-F at 6 s and 25 s, respectively. We find that the $\langle S_e \rangle$ is larger than the $\langle S_k \rangle$ and the PDFs of S_e and S_k overlap at 6 s (Fig.

12(a)). Hence, growth is always positive and activation is mean-dominated[43] for particles that experience $\langle S_e \rangle > \langle S_k \rangle$. But fluctuation-influenced[43] activation or deactivation occurs in the overlapping region. Particles, that have radii closer to the critical radii, will activate or deactivate if fluctuations are positive or negative, respectively. At 25 s, the $\langle S_e \rangle$ is equal to the $\langle S_k \rangle$ while the PDFs overlap (Fig. 12(b)). Since there is no difference between the mean supersaturation values, activation or deactivation is dominated by fluctuations in the S_e and S_k.[43]

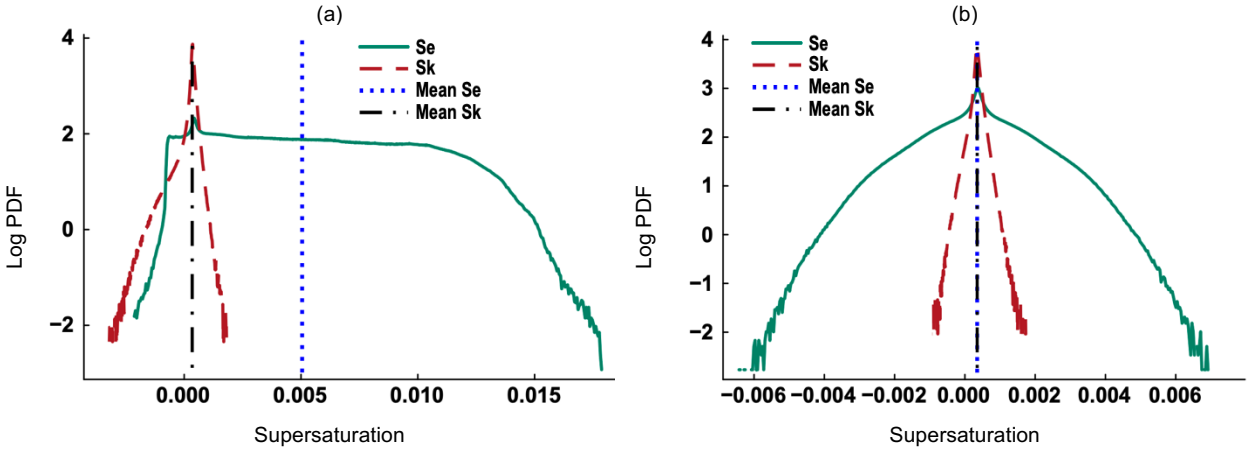

FIG. 12 Log PDFs of instantaneous supersaturation for Case L-F at (a) 6 s and (b) 25 s in Study I. Case L-F implements scalar forcing in the Fourier space. The turbulence level is 'low' for both cases. The vertical lines represent mean values in respective PDFs.

Cloud and aerosol microphysics differ for the unforced and forced cases. Figures 13(a)-(c) show the PDFs of particle radii (f_r) for Case L during condensation (Study I) at 0 s, 3 s, and 10 s, respectively. Figures 13(d)-(e) are analogous to Figs. 13(b)-(c) but represent Case L-MGF. Lognormally distributed dry aerosol particles are present at 0 s (Fig. 13(a)) for both cases. By 3 s, some of the aerosol particles activate into cloud droplets and the f_r of aerosol particles broaden for Case L (Fig. 13(b)). Between 3 s to 15 s, particles grow further, and the mean radii of aerosol particles and cloud droplets increase (Fig. 13(c)). The increase of particle radius and broadening of f_r are also evident for Case L-MGF (Figs. 13(d)-(e)). The f_r of cloud droplets and aerosol particles for Case L are skewed to the left. Thus, some cloud droplets and aerosol particles are much smaller than their mean values. Interestingly, the f_r of cloud droplets are skewed to the right at 15 s for Case L-MGF (Fig. 13(e)). The maximum radius is much larger for this case (13.5 μm) than that for Case L (5.1 μm). Therefore, some cloud droplets experience super-adiabatic growth[44] when mean gradient forcing is applied. However, extreme growth of some droplets is accompanied by reduced growth of other droplets. For example, the mean and minimum radii of cloud droplets for Case L-MGF are smaller than those for Case L at 15 s.

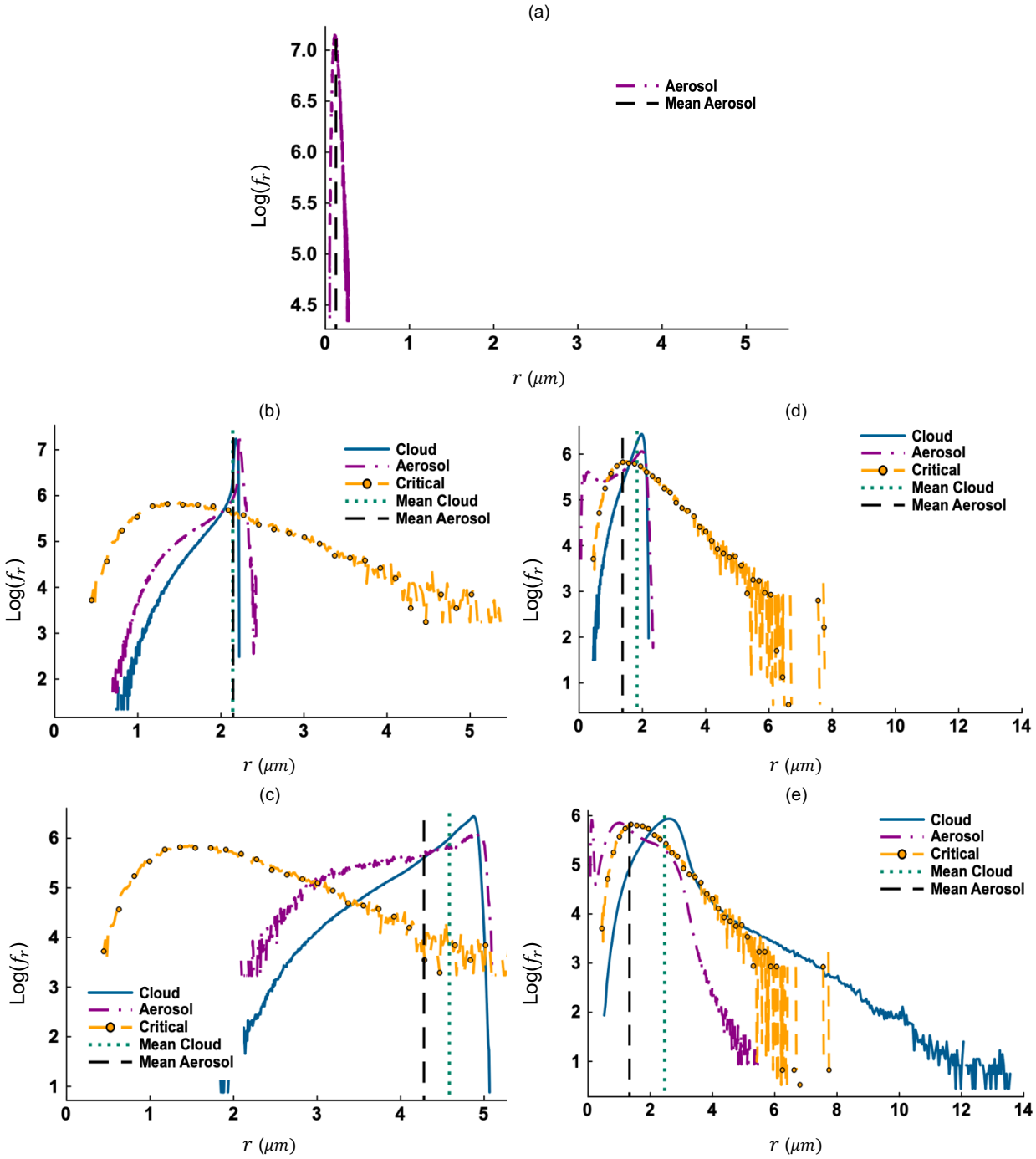

FIG. 13 (a) Log PDF of dry aerosol radii at 0 s. Log PDFs of particle size at (b) 3 s and (c) 15 s for Case L in Study I. Log PDFs of particle size at (d) 3 s and (e) 15 s for Case L-MGF in Study I. The curve with 'circle' mark shows the critical radius (r_c) distribution. Scalar forcing is absent in Case L. Case L-MGF applies mean gradient forcing and calculates the β adaptively.

2. *Deactivation of cloud droplets*

The fraction of cloud droplets that deactivate into aerosol particles with time is shown in Fig. 14(a). We see that deactivation fraction is maximum for the unforced case (L). Figure 14(b) shows the time evolution of mean radius

during evaporation. The mean radius decreases most for Case L and least for Case L-MGF. Scalar forcing slows down phase change and evaporative decay in Study II. The profiles in Fig. 14(b) and Fig. 14(a) are apparently in opposite order. As droplet radii decrease by evaporation, the deactivation fraction goes up. Figures 15(a)-(b) are analogous to Figs. 12(a)-(b) but based on the data from Study II. For particles experiencing $\langle S_e \rangle < \langle S_k \rangle$ at 10 s (Fig. 15(a)), growth is always negative, and deactivation is mean-dominated. Also, the PDFs of S_e and S_k overlap (Fig. 15(a)), leading to fluctuation-influenced activation or deactivation in the overlapping region. The $\langle S_e \rangle$ is very close to the $\langle S_k \rangle$ at 25 s (Fig. 15(b)) and the two PDFs overlap. As a result, activation or deactivation is fluctuation-dominated at 25 s.

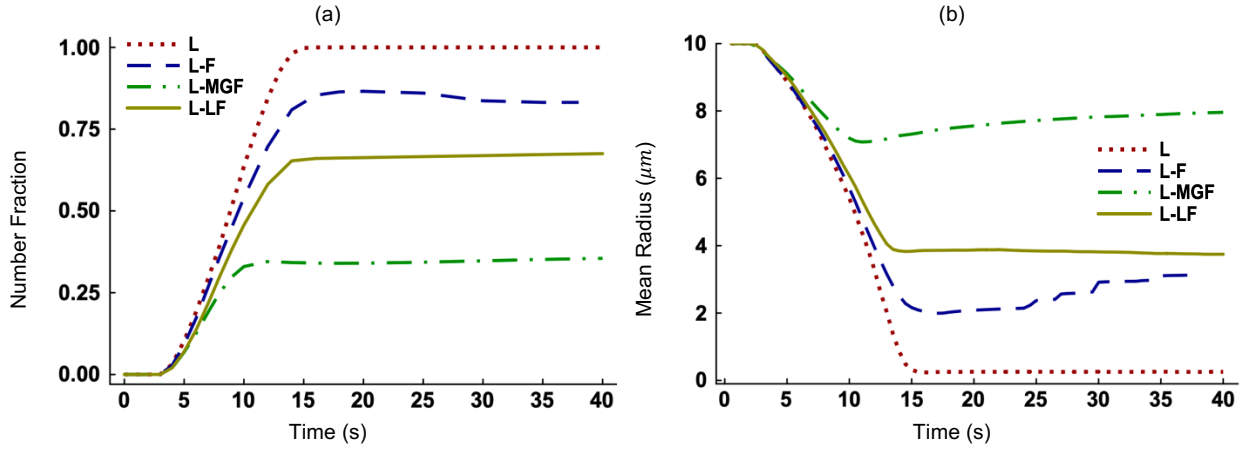

FIG. 14 Time evolution of the (a) number of deactivated cloud droplets, and (b) mean radius of all particles, in Study II. Scalar forcing is absent in Case L. Case L-F implements scalar forcing in the Fourier space. Case L-MGF applies mean scalar gradient forcing and Case L-LF has linear scalar forcing. The turbulence level is 'low' for all cases.

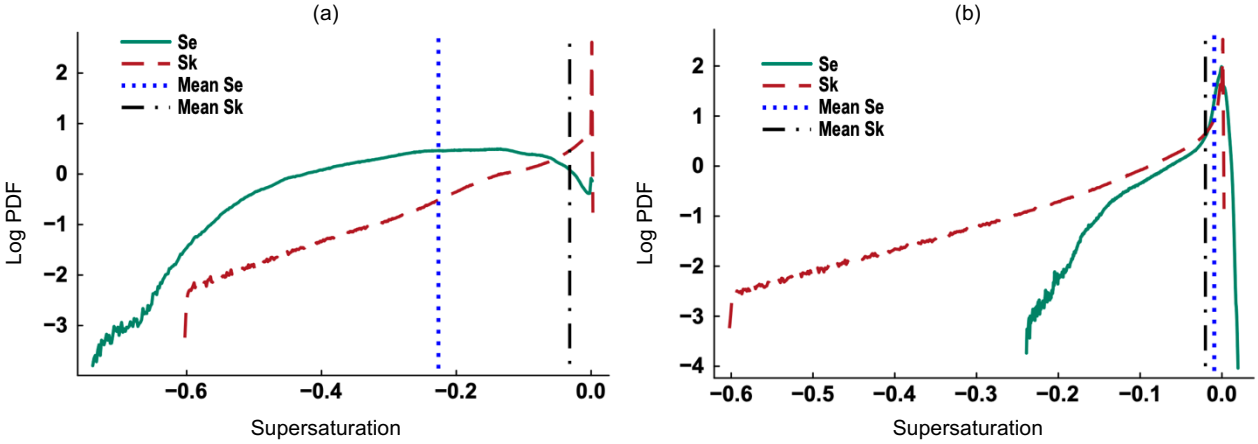

FIG. 15 Log PDFs of instantaneous supersaturation for Case L-F at (a) 10 s and (b) 25 s in Study II. Case L-F implements scalar forcing in the Fourier space. The turbulence level is 'low' for both cases.

The PDFs of particle radii (f_r) are shown in Figs. 16(a)-(e) at three selected times in Study II. As dry subsaturated air mixes with the cloud volume, the mean radii of initially monodisperse (10 μm) cloud droplets (Fig. 16(a)) decrease between 0 s to 5 s for Cases L (Figs. 16(b)) and L-LF (Fig. 16(d)). The f_r of cloud droplets broadens and is skewed to

the left for both cases at 5 s. On the other hand, the f_r of aerosol particles is skewed to the right. Between 5 s to 15 s, the mean droplet radii decrease for both cases, and the f_r of cloud droplets narrows for Case L (Fig. 16(c)) but not for Case L-LF (Fig. 16(e)). Because of strong evaporation, smaller cloud droplets evaporate completely while larger ones shrink in size when scalar fields are not forced (Case L). By 15 s, the mean droplet radii decrease less for Case L-LF ($\sim 6\ \mu m$) compared to that for Case L ($\sim 3\ \mu m$) since forcing slows down evaporation. Bimodality in the f_r of aerosol particles is evident for both cases, with one peak for smaller aerosol particles and another peak for larger particles. The bimodal size distribution of aerosol particles[45] and the coexistence of aerosols and cloud droplets[46] are observed in natural clouds.

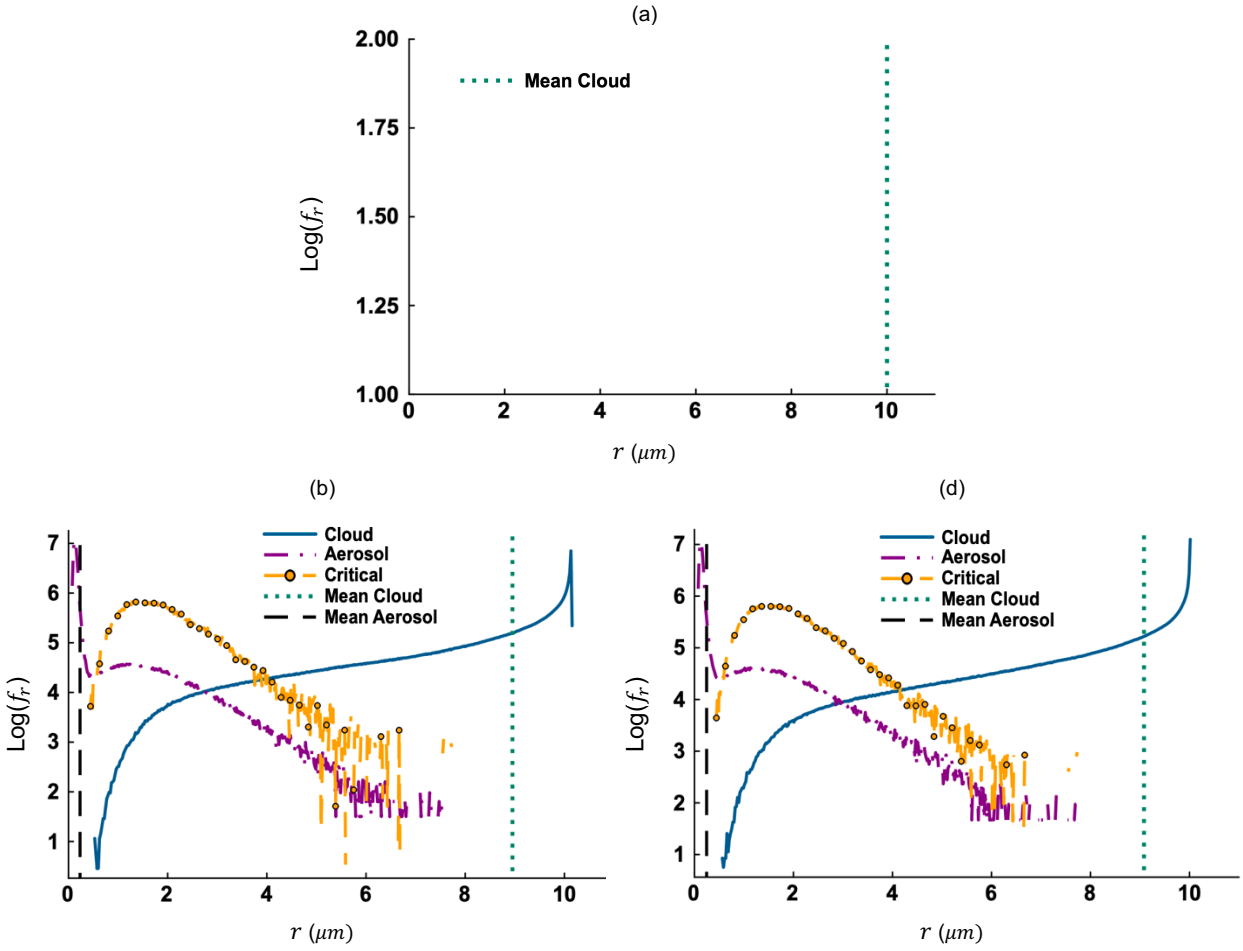

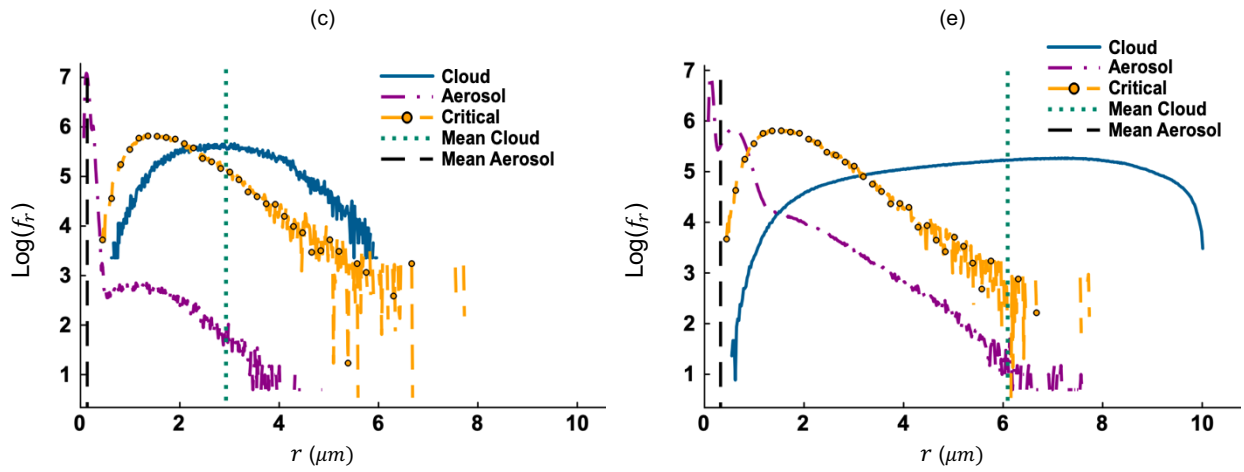

FIG. 16 (a) Log PDF of cloud droplet radii at 0 s. Log PDFs of particle size at (b) 5 s and (c) 15 s for Case L in Study II. Log PDFs of particle size at (d) 5 s and (e) 15 s for Case L-LF in Study II. The curve with 'circle' mark shows the critical radius (r_c) distribution. Scalar forcing is absent in Case L. Case L-LF applies linear scalar forcing and calculates the α adaptively.

C. Flow turbulence, scalar forcing, and microphysics

We simulate Cases H and H-F, where 'H' denotes high flow turbulence level and 'F' denotes scalar forcing in the Fourier space. Figure 17(a) compares the variances of vapor mixing ratio $\sigma_{q_v}^2$ for Cases L, H, L-F, and H-F. The $\sigma_{q_v}^2$ decays faster for Case H compared to Case L. In absence of scalar forcing, higher velocity turbulence homogenizes the scalar fields[6] and reduces fluctuations in the vapor mixing ratio and temperature. When scalar forcing is applied (Cases L-F and H-F), it counteracts turbulent homogenization and the $\sigma_{q_v}^2$ becomes statistically stationary (Fig. 17(a)). The spectra of fluctuating vapor mixing ratio are plotted in Figure 17(b). They appear to converge at the small scales for Cases L and H. But fluctuations increase significantly at the small scales for the forced cases (L-F and H-F). The PDFs of fluctuating z-velocity ($f_{w'}$) and fluctuating environmental supersaturation ($f_{S_e'}$) are shown in Figs. 18(a)-(b), respectively. The $f_{w'}$ for Cases H and H-F are found to be broader than those for Cases L and L-F (Fig. 18(a)). Such broadening is caused by high flow turbulence. The $f_{w'}$ are identical for Cases L and L-F, and for Cases H and H-F because scalar fields and particles do not influence the velocity field in our model.[6] The PDFs of x- and y-velocities resemble those of z-velocity as turbulence is isotropic. The $f_{S_e'}$ is narrower for Cases L and H compared to the forced cases (Fig. 18(b)) as fluctuations decay without forcing. We also see that the peaks are sharp for the $f_{S_e'}$ but rounded for the $f_{w'}$.

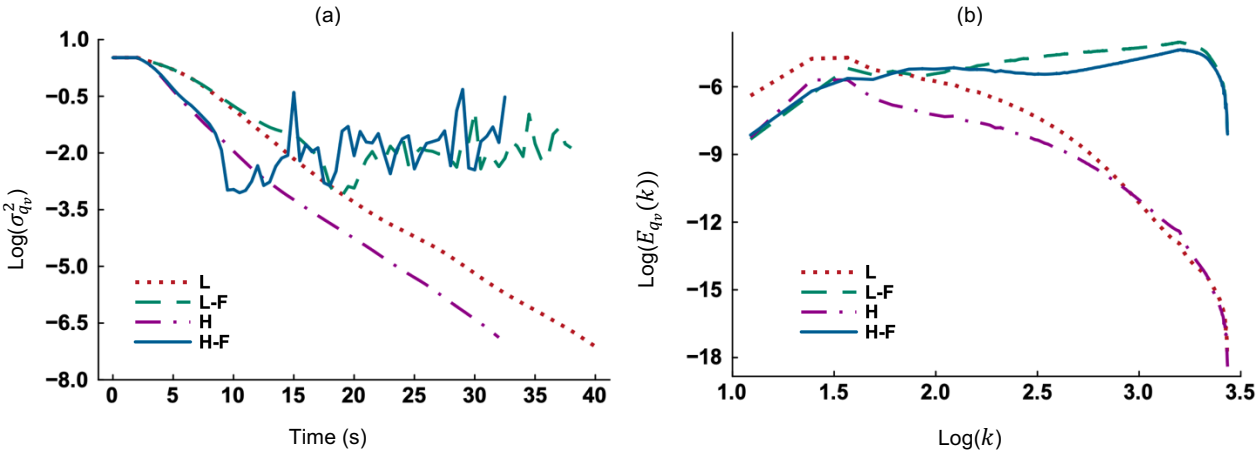

FIG. 17 (a) Time evolution of the variance of fluctuating vapor mixing ratio in Study II and (b) Spectra of fluctuating vapor mixing ratio field at 25 s in Study II. Scalar forcing is absent in Cases L and H. Cases L-F and H-F apply scalar forcing in the Fourier space with 'low' and 'high' velocity turbulence levels, respectively.

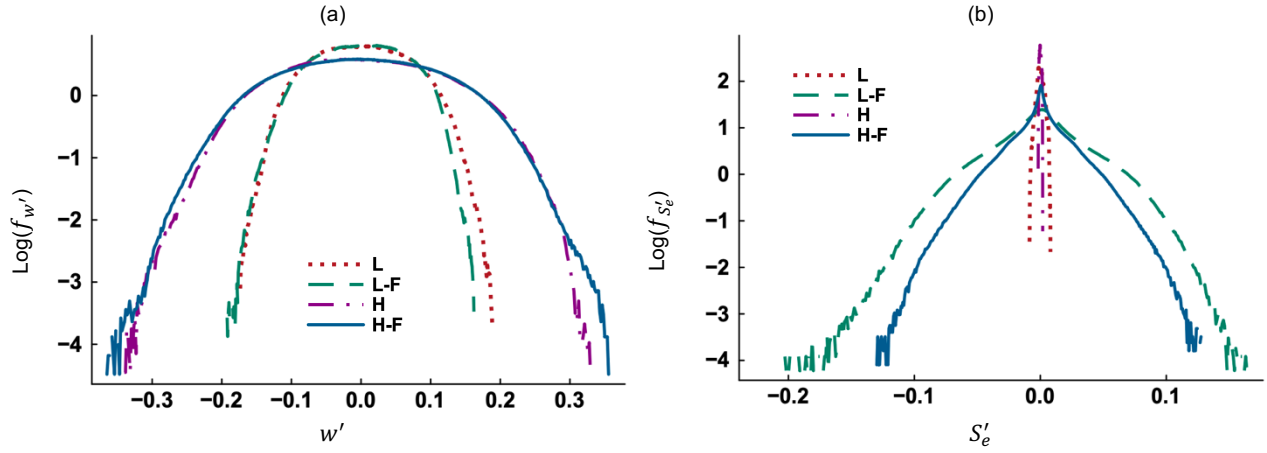

FIG. 18 Log PDFs of the (a) fluctuating z-velocity (w') and (b) fluctuating environmental supersaturation (S_e') at 25 s in Study II.

Both momentum forcing (flow turbulence) and scalar forcing affect the microscale evolution of aerosols and cloud droplets. Figures 19(a)-(b) report the standard deviations of particle radius (σ_r) in Studies I and II, respectively. As particles are released in the model domain, turbulence broadens the size distribution of particles[47] and increases the σ_r initially for all cases (Figs. 19(a)-(b)). The σ_r is smaller for Case H compared to Case L in both figures as high flow turbulence spreads out microphysical fluctuations. With scalar forcing, the σ_r increases if the turbulence level is low (L-F) but decreases when the latter is high (H-F) compared to the respective unforced cases (L and H) in Study I (Fig. 19(a)). In Study II, the σ_r decays completely for Cases L and H as cloud droplets shrink and the r approaches zero (Fig. 19(b). The decay is rather prevented for the forced cases (L-F and H-F). These results demonstrate that momentum and scalar forcings cause variation in thermodynamic fluctuations which in turn significantly influence microphysical fluctuations.

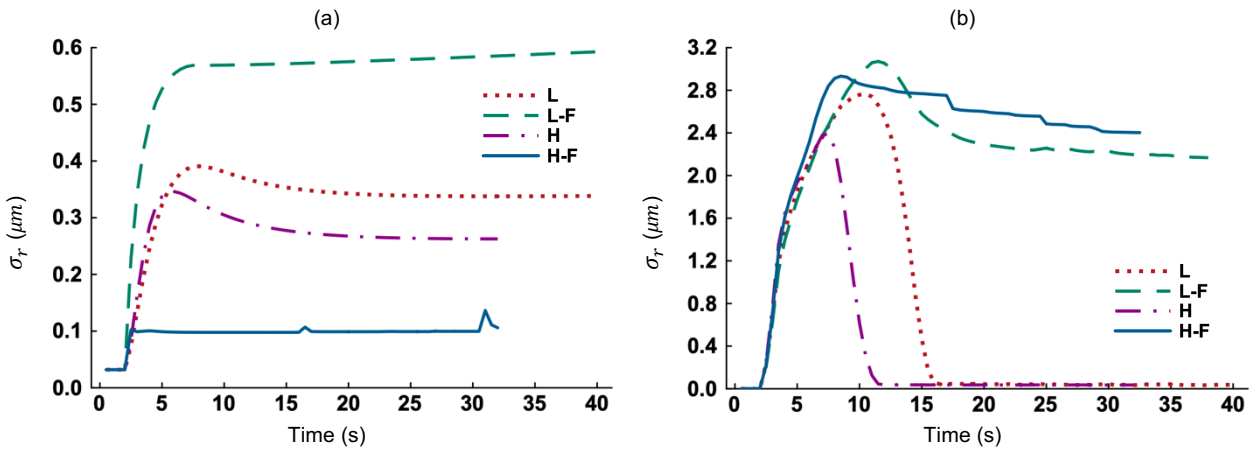

FIG. 19 Standard deviation of particle radius (σ_r) in (a) Study I, and (b) Study II. Scalar forcing is absent in Cases L and H. Cases L-F and H-F apply scalar forcing in the Fourier space with 'low' and 'high' velocity turbulence levels, respectively.

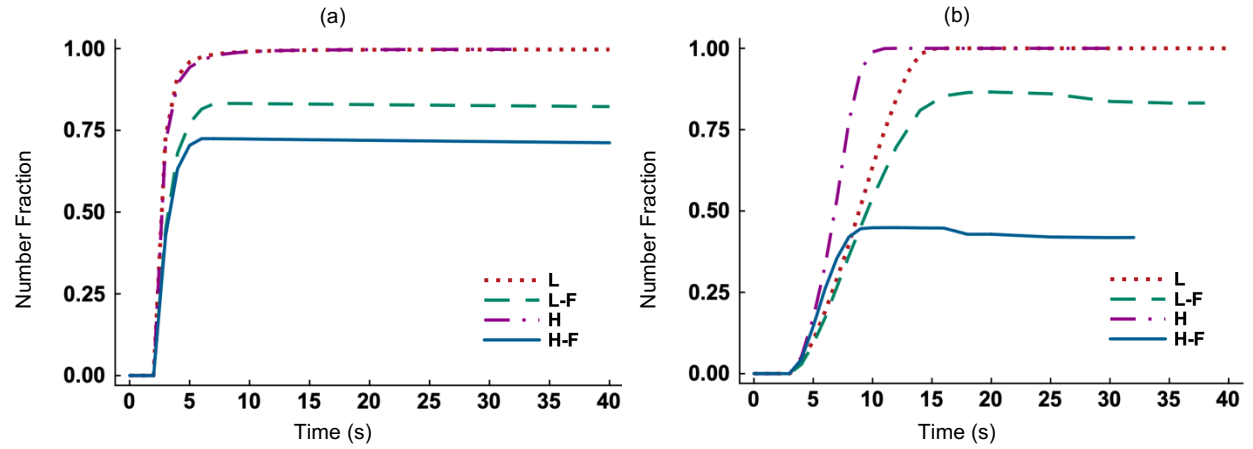

FIG. 20 Time evolution of the (a) number fraction of activated aerosol particles in Study I and (b) number fraction of deactivated cloud droplets in Study II. Scalar forcing is absent in Cases L and H. Cases L-F and H-F apply scalar forcing in the Fourier space with 'low' and 'high' velocity turbulence levels, respectively.

Figure 20(a) shows the number fractions of activated aerosol particles for the four cases. The activation fraction is slightly smaller for Case H compared to Case L between 3 s to 7 s. Higher turbulence leads to stronger mixing and causes most particles to grow evenly instead of some particles growing fast and crossing the activation barrier. Thus, activation fraction is reduced if the turbulence level is high and scalar forcing is absent (Case H). At long time, the activation fractions for Cases L and H are identical. We also see in Fig. 20(a) that fewer aerosol particles activate into cloud droplets for the forced cases (H-F and L-F) compared to the unforced cases (H and L). As scalar forcing leads the system towards equilibrium faster, it suppresses phase change events like condensation (activation) in our model. The deactivation profiles in Fig. 20(b) show that deactivation is faster for Case H compared to Case L. Because of homogenization, more cloud droplets experience partial evaporation rather than some of them evaporating fully. This increases the number of cloud droplets that shrink below the critical radii and deactivate in Case H. Again, scalar

forcing slows down phase change (evaporation) in Study II and reduces deactivation fraction. It is evident that both activation and deactivation fractions are smaller for Case H-F compared to Case L-F (Figs. 20(a)-(b)). This is because scalar forcing weakens phase change further when the turbulence level is high and mixing is rapid.

V. CONCLUDING REMARKS

Using a three-dimensional finite difference based direct numerical simulation (DNS) model, we have examined the role of scalar forcing during condensation (activation) and evaporation (deactivation). The key findings from our simulations are itemized below.

- The mean and fluctuating scalar fields evolve from nonzero initial conditions. Forcing of the scalar fields leads scalar fluctuations to statistical stationarity (Figs. 3 and 7) and drives mean scalar fields to equilibrium faster (Figs. 5 and 10).
- While dissipation rates in the initial scalar fields are known, the mean scalar gradient β and the scalar variance α are not known a priori. Hence, it is easier to control the magnitude of forcing using the Fourier method than the other two methods. The magnitude of forcing is higher with mean gradient forcing compared to Fourier and linear forcings in our model.
- Unlike the mean velocity field, the mean scalar fields are not zero in our model. Hence, forcing increases the rate of change in the mean scalar fields. The physical analogue is rapid change in the mean temperature and vapor mixing ratio during intense mixing between cloud and environment, updrafts and downdrafts.[48]
- The scalar fields, when coupled with particles, have reduced diffusivity and higher Scmidt number. Also, their spectral profiles include a viscous-convective regime (Figs. 4(a)-(b)) that falls between the inertial-convective and dissipation ranges. The spectra of unforced and forced scalar fields differ at the intermediate and small scales because forcing makes the viscous-convective regime dominant.
- No phase changes (condensation and evaporation) occur, and the mean vapor mixing ratio remains unchanged with time (Fig. 6(a)) in absence of particles. Scalar forcing does not cause deviation from homogeneity and isotropy in the scalar fields if particles are absent (Fig. 6(b)).
- The PDFs of fluctuating scalar fields have high kurtosis and are not Gaussian if forcing is applied (Fig. 9). Mean gradient forcing produces extreme fluctuations in our model leading to super-adiabatic droplet growth (Fig. 13(e)) which is often observed in stratocumulus clouds.[44]

- Scalar forcing reduces the time available for phase change. So, condensational growth is suppressed (Fig. 11(b)) and fewer aerosol particles activate into cloud droplets (Fig. 11(a)). Similarly, evaporation is suppressed (Fig. 14(b)) and fewer cloud droplets deactivate into aerosol particles (Fig. 14(a)).
- Activation and deactivation are mean-dominated at early times (Figs. 12(a) and 15(a)). At long time, activation and deactivation are fluctuation-dominated (Figs. 12(b) and 15(b)) if scalar forcing is present.
- Higher velocity turbulence homogenizes the scalar fields if scalar forcing is absent. On the other hand, scalar forcing counteracts turbulent homogenization (Fig. 17(a)). Both flow turbulence and scalar forcing influence the microphysics of cloud droplets and aerosols (Figs. 19 and 20).
- The magnitude of thermodynamic fluctuations varies in natural clouds.[39] A numerical model with scalar forcing can maintain thermodynamic fluctuations at desired levels and is suitable to study microscale events in a cloudy region where these fluctuations are strong.

ACKNOWLEDGEMENTS

This research used resources of the National Energy Research Scientific Computing Center (NERSC), a Department of Energy Office of Science User Facility using NERSC award NERSC ASCR-ERCAP0027399. We acknowledge support from the LDRD program at Brookhaven National Laboratory, which is sponsored by the US Department of Energy, Office of Science, under Contract Number DE-SC0012704. This project was partially funded by 2022 Stony Brook University (SBU) - Brookhaven National Laboratory (BNL) Seed Grant Program Award #: 94508.

DATA AVAILABILITY

The data that support the findings of this work are available from the corresponding author upon reasonable request.

[1]P. Vaillancourt, "Microscopic approach to cloud droplet growth by condensation," Ph.D. Thesis, McGill University, Montreal, Quebec, 1998.

[2]V. Eswaran, and S.B. Pope, "An examination of forcing in direct numerical simulations of turbulence," *Computers & Fluids*, *16*(3), pp.257-278 (1988).

[3]B. Kumar, J. Schumacher, and R.A. Shaw, "Lagrangian mixing dynamics at the cloudy–clear air interface," *Journal of the Atmospheric Sciences*, *71*(7), pp.2564-2580 (2014).

[4]X.Y. Li, "Droplet growth in atmospheric turbulence: A direct numerical simulation study," Ph.D. Thesis, Stockholm University, Stockholm, 2018.

[5]Z. Gao, Y. Liu, X. Li, and C. Lu, "Investigation of turbulent entrainment-mixing processes with a new particle-resolved direct numerical simulation model," *Journal of Geophysical Research: Atmospheres*, *123*(4), 2194-2214 (2018).

[6]A.A.M. Sharfuddin, F. Ladeinde, Y. Liu, M. Atif, F. Yang, V. Lopez-Marrero, M. Lin, and T. Zhang, "Direct numerical simulations of activation and deactivation in turbulent atmospheric clouds," Under review in *Physics of Fluids* (2025).

[7]W.W. Grabowski, Y. Kim, and S.S. Yum, "CCN Activation and Droplet Growth in Pi Chamber Simulations with Lagrangian Particle–Based Microphysics," *Journal of the Atmospheric Sciences*, *81*(7), pp.1201-1212 (2024).

[8]J. Janin, F. Duval, C. Friess, and P. Sagaut, "A new linear forcing method for isotropic turbulence with controlled integral length scale," *Physics of Fluids*, *33*(4) (2021).

[9]M.R. Overholt, and S.B. Pope, "Direct numerical simulation of a passive scalar with imposed mean gradient in isotropic turbulence," *Physics of Fluids*, *8*(11), pp.3128-3148 (1996).

[10]T. Gotoh, and T. Watanabe, "Scalar flux in a uniform mean scalar gradient in homogeneous isotropic steady turbulence," *Physica D: Nonlinear Phenomena*, *241*(3), pp.141-148 (2012).

[11]D. Daniel, D. Livescu, and J. Ryu, "Reaction analogy based forcing for incompressible scalar turbulence," *Physical Review Fluids*, *3*(9), p.094602 (2018).

[12]S. Chen, and N. Cao, "Anomalous scaling and structure instability in three-dimensional passive scalar turbulence," *Physical Review Letters*, *78*(18), p.3459 (1997).

[13]T. Watanabe, and T. Gotoh, "Statistics of a passive scalar in homogeneous turbulence," *New Journal of Physics*, *6*(1), p.40 (2004).

[14]R.M. Kerr, "Higher-order derivative correlations and the alignment of small-scale structures in isotropic numerical turbulence," *Journal of Fluid Mechanics*, *153*, pp.31-58 (1985).

[15]P. L. Carroll, S. Verma, and G. Blanquart, "A novel forcing technique to simulate turbulent mixing in a decaying scalar field," *Physics of Fluids*, *25*(9) (2013).

[16]R. Paoli, and K. Shariff, "Turbulent condensation of droplets: Direct simulation and a stochastic model," *Journal of the atmospheric sciences*, *66*(3), pp.723-740 (2009).

[17]S. Chen, L. Xue, S. Tessendorf, K. Ikeda, C. Weeks, R. Rasmussen, M. Kunkel, D. Blestrud, S. Parkinson, M. Meadows, and N. Dawson, "Mixed-phase direct numerical simulation: ice growth in cloud-top generating cells," *Atmospheric Chemistry and Physics*, *23*(9), pp.5217-5231 (2023).

[18]I. Saito, T. Watanabe, and T. Gotoh, "Spectrum of passive scalar carried by particles in isotropic turbulence," *Physical Review Fluids*, *9*(5), p.054601 (2024).

[19]A. Pumir, "A numerical study of the mixing of a passive scalar in three dimensions in the presence of a mean gradient," *Physics of Fluids*, *6*(6), pp.2118-2132 (1994).

[20]K. Zhou, A. Attili, A. Alshaarawi, and F. Bisetti, "Simulation of aerosol nucleation and growth in a turbulent mixing layer," *Physics of Fluids*, *26*(6) (2014).

[21]M. Andrejczuk, W.W. Grabowski, S.P. Malinowski, and P.K. Smolarkiewicz, "Numerical simulation of cloud–clear air interfacial mixing," *Journal of the atmospheric sciences*, *61*(14), 1726-1739 (2004).

[22]D. Carati, S. Ghosal, and P. Moin, "On the representation of backscatter in dynamic localization models," *Physics of Fluids*, *7*(3), 606-616 (1995).

[23]B.E. Harrop, and D.L. Hartmann, "The role of cloud radiative heating within the atmosphere on the high cloud amount and top-of-atmosphere cloud radiative effect," *Journal of Advances in Modeling Earth Systems*, *8*(3), pp.1391-1410 (2016).

[24]M.D. Petters, and S.M. Kreidenweis, "A single parameter representation of hygroscopic growth and cloud condensation nucleus activity," *Atmospheric Chemistry and Physics*, *7*(8), 1961-1971 (2007).

[25]R. West, "The parameterisation of microphysical cloud droplet formation in the Met Office Unified Model," (2009).

[26]D.D.A. Rothenberg, "Fundamental aerosol-cloud interactions and their influence on the aerosol indirect effect on climate," Ph.D. Thesis, Massachusetts Institute of Technology, Boston, 2017.

[27]D. Newth, and D. Gunasekera, "Projected changes in wet-bulb globe temperature under alternative climate scenarios," *Atmosphere*, *9*(5), 187 (2018).

[28]F. Yang, P. Kollias, R.A. Shaw, and A.M. Vogelmann, "Cloud droplet size distribution broadening during diffusional growth: ripening amplified by deactivation and reactivation," *Atmospheric Chemistry and Physics*, *18*(10), 7313-7328 (2018).

[29]C. Rosales, and C. Meneveau, "Linear forcing in numerical simulations of isotropic turbulence: Physical space implementations and convergence properties," *Physics of fluids*, *17*(9) (2005).

[30]W.W. Grabowski, and H. Morrison, "Supersaturation, buoyancy, and deep convection dynamics," *Atmospheric Chemistry and Physics*, *21*(18), pp.13997-14018 (2021).

[31]B. Kumar, J. Schumacher, and R.A. Shaw, "Lagrangian mixing dynamics at the cloudy–clear air interface," *Journal of the Atmospheric Sciences*, *71*(7), pp.2564-2580 (2014).

[32]D. Rose, S.S. Gunthe, E. Mikhailov, G.P. Frank, U. Dusek, M.O. Andreae, and U. Pöschl, "Calibration and measurement uncertainties of a continuous-flow cloud condensation nuclei counter (DMT-CCNC): CCN activation of ammonium sulfate and sodium chloride aerosol particles in theory and experiment," *Atmospheric Chemistry and Physics*, *8*(5), 1153-1179 (2008).

[33]F. Ladeinde and, H. Oh, "Stochastic and spectra contents of detonation initiated by compressible turbulence thermodynamic fluctuation," *Physics of Fluids 33, 045111* (2021).

[34]S.B. Pope, *Turbulent flows* (Cambridge University Press, Cambridge, 2000).

[35]R.A. Antonia, and P. Orlandi, "Effect of Schmidt number on small-scale passive scalar turbulence," *Appl. Mech. Rev.*, *56*(6), pp.615-632 (2003).

[36]P.K. Yeung, S. Xu, D.A. Donzis, and K.R. Sreenivasan, "Simulations of three-dimensional turbulent mixing for Schmidt numbers of the order 1000," *Flow, turbulence and combustion*, *72*, pp.333-347 (2004).

[37]F. Ditas, R.A. Shaw, H. Siebert, M. Simmel, B. Wehner and A. Wiedensohler, "Aerosols-cloud microphysics-thermodynamics-turbulence: evaluating supersaturation in a marine stratocumulus cloud," *Atmospheric Chemistry and Physics*, *12*(5), 2459-2468 (2012).

[38]F. Yang, R. McGraw, E.P. Luke, D. Zhang, P. Kollias, and A.M. Vogelmann, "A new approach to estimate supersaturation fluctuations in stratocumulus cloud using ground-based remote-sensing measurements," *Atmospheric Measurement Techniques*, *12*(11), pp.5817-5828 (2019).

[39]S. Thomas, P. Prabhakaran, W. Cantrell, and R.A. Shaw, "Is the water vapor supersaturation distribution Gaussian?," *Journal of the Atmospheric Sciences*, *78*(8), pp.2385-2395 (2021).

[40]J. Fries, G. Sardina, G. Svensson, A. Pumir, and B. Mehlig, "Lagrangian supersaturation fluctuations at the cloud edge," *Physical Review Letters*, *131*(25), p.254201 (2023).

[41]B. Kumar, R. Ranjan, M.K. Yau, S. Bera, and S.A. Rao, "Impact of high and low vorticity turbulence on cloud environment mixing and cloud microphysics processes," *Atmospheric Chemistry and Physics Discussions*, *2021*, pp.1-17 (2021).

[42]A.A.M. Sharfuddin, F. Ladeinde, Y. Liu, F. Yang, T. Zhang, M. Atif, M. Lin, and V. Lopez-Marrero, "The impact of scalar forcing on cloud microphysics based on direct numerical simulations," AIAA Paper No. 2025-2223, 2025.

[43]P. Prabhakaran, A.S.M. Shawon, G. Kinney, S. Thomas, W. Cantrell, and R.A. Shaw, "The role of turbulent fluctuations in aerosol activation and cloud formation," *Proceedings of the National Academy of Sciences*, *117*(29), pp.16831-16838 (2020).

[44]F. Yang, R. Shaw, and H. Xue, "Conditions for super-adiabatic droplet growth after entrainment mixing," *Atmospheric Chemistry and Physics*, *16*(14), pp.9421-9433 (2016).

[45]S. Ueda, K. Miura, R. Kawata, H. Furutani, M. Uematsu, Y. Omori, and H. Tanimoto, "Number–size distribution of aerosol particles and new particle formation events in tropical and subtropical Pacific Oceans," *Atmospheric environment*, *142*, pp.324-339 (2016).

[46]A.S.M. Shawon, P. Prabhakaran, G. Kinney, R.A. Shaw and W. Cantrell, "Dependence of Aerosol-Droplet Partitioning on Turbulence in a Laboratory Cloud," *Journal of Geophysical Research: Atmospheres*, *126*(5), e2020JD033799 (2021).

[47]M.J. Manton, "On the broadening of a droplet distribution by turbulence near cloud base," *Quarterly Journal of the Royal Meteorological Society*, *105*(446), pp.899-914 (1979).

[48]R.A. Shaw, "Supersaturation intermittency in turbulent clouds," *Journal of the atmospheric sciences*, *57*(20), pp.3452-3456 (2000).